lubricants

MDPI

Review

Structural Superlubricity of Two-Dimensional Materials: Mechanisms, Properties, Influencing Factors, and Applications

Fan-Bin Wu, Sheng-Jian Zhou, Jia-Hu Ouyang *, Shu-Qi Wang and Lei Chen

School of Materials Science and Engineering, Harbin Institute of Technology, Harbin 150001, China
* Correspondence: ouyangjh@hit.edu.cn

Abstract: Structural superlubricity refers to the lubrication state in which the friction between two crystalline surfaces in incommensurate contact is nearly zero; this has become an important branch in recent tribological research. Two-dimensional (2D) materials with structural superlubricity such as graphene, MoS_2, *h*-BN, and alike, which possess unique layered structures and excellent friction behavior, will bring significant advances in the development of high-performance micro-electromechanical systems (MEMS), as well as in space exploration, space transportation, precision manufacturing, and high-end equipment. Herein, the review mainly introduces the tribological properties of structural superlubricity among typical 2D layered materials and summarizes in detail the underlying mechanisms responsible for superlubricity on sliding surfaces and the influencing factors including the size and layer effect, elasticity effect, moiré superlattice, edge effect, and other external factors like normal load, velocity, and temperature, etc. Finally, the difficulties in achieving robust superlubricity from micro to macroscale were focused on, and the prospects and suggestions were discussed.

Keywords: structural superlubricity; incommensurate contact; two-dimensional materials; elasticity effect; moiré superlattices; micro to macroscale

Citation: Wu, F.-B.; Zhou, S.-J.; Ouyang, J.-H.; Wang, S.-Q.; Chen, L. Structural Superlubricity of Two-Dimensional Materials: Mechanisms, Properties, Influencing Factors, and Applications. *Lubricants* **2024**, *12*, 138. https://doi.org/10.3390/lubricants12040138

Received: 18 March 2024
Revised: 14 April 2024
Accepted: 16 April 2024
Published: 18 April 2024

1. Introduction

Friction and wear phenomena are everywhere in the industrial field, constantly affecting the mechanical and physical properties of components in sliding and rolling contact. For the entire industrial system, friction and wear resulting in energy loss and economic loss is an important problem in the industrial field that cannot be ignored [1]. According to incomplete statistics, the primary energy loss caused by friction and wear accounts for about 20 to 30% of the world's total, of which about 80% of the mechanical parts and components are due to friction and wear failure. The annual economic losses generated by friction and wear and tear in most countries account for 2 to 7% of GDP [1–3]. Reducing the harmful effects of friction and wear in the industry through advanced tribological technologies would reduce CO_2 emissions by more than 1 billion tons of CO_2 worldwide in a short period, with cost savings of more than 4 billion euros [2,4]. In today's society, there is a growing focus on green development to achieve carbon peak and carbon neutrality. Therefore, promoting the development and innovation of friction-reducing and wear-resistant technologies is very crucial.

The introduction of 'superlubricity' represents a significant advancement in the quest to minimize friction and wear. In 1993, Shinjo and Hirano investigated the kinetic nature of friction from an atomic point of view and introduced the concept of 'superlubricity' for the first time, which is a state where the lateral friction between two incommensurate crystal contact surfaces almost vanishes [5]. This discovery extended the study of friction and wear from the macro to the microscale. With the development of precision instruments and small-scale components, the scope of research expanded from bearings and lubrication of

large mechanical components to microelectromechanical systems (MEMS) and other micro-precision devices [6]. In contrast to the phenomena of superconductivity and superfluidity, superlubricity still involves the dissipation of frictional energy between the frictional parts, which is typically due to a dissipation mechanism of the electron-phonon coupling [4]. The coefficient of friction in the state of structural superlubricity is typically on the order of 10^{-3} or lower [7].

Over the past 30 years, the concept of superlubricity has been extensively developed. Currently, there are three main types of superlubricity: solid superlubricity, liquid superlubricity, and compound superlubricity in solid-liquid systems. Solid superlubricity materials are mainly one-dimensional and 2D layered materials, such as carbon nanotubes (CNTs), graphite, graphene, transition metal dichalcogenides (TMDs), and *h*-BN. Some materials achieve superlubricity via the mechanism of structural superlubricity, which has been used in MEMS as ultra-wear-resistant nanocomponents [6,8]; exceptionally, amorphous carbon materials like diamond-like carbon (DLC) have also exhibited superlubricity due to their tribochemistry-induced allotropic transitions [9], such as α-C to α-C: H transitions [10] or surface-localized sp^2 hybridization [11], which form tribochemical films on the surface. Liquid superlubricity involves using acidic solvents, such as phosphoric acid and salicylic acid, as well as ionic liquids, which have been used in medical devices such as tracheal intubation [12]. These substances combine with the lubricant to form a hydrated layer, which is assisted by the acid and relies on a hydrodynamic mechanism to achieve superlubricity [13]. The superlubricity of a solid-liquid system involves the auxiliary role of 2D layered materials in liquid lubrication. These materials have very low shear strength and strong hydrophilicity, which allows for the formation of a hydration layer that can be easily sheared, resulting in a significant reduction in frictional resistance and an increase in carrying capacity [13,14].

The discovery of structural superlubricity predates the concept of superlubricity by 10 years [15]. With the development of superlubricity, scientists have found that there are many ways to achieve near-zero friction in the process of exploring the phenomenon of superlubricity. Müser referred to the state of near-zero friction between incommensurate contacts of two rigid crystals as 'structural superlubricity' [16]. Since the investigation of structural superlubricity, the theoretical system has gradually improved, leading to positive repercussions in the field of nanofriction. Important contributions have been made by several research groups such as Dietzel et al. [17] and Zheng et al. [18] in characterizing the structural superlubricity phenomena, developing nanofriction testing techniques, and proposing the underlying mechanisms.

Structural superlubricity is expected to achieve robust lubrication for an extended period because it does not require additional lubricant from outside sources [19]. The two contact surfaces have a unique structure that eliminates the need for lubricant replenishment. Therefore, structural superlubricity is currently one of the most promising solutions for achieving superlubricity from a long-term perspective.

Since the discovery of structural superlubricity properties in single-crystal graphite flakes, the development of 2D materials for tribological applications has gradually begun [20]. Two-dimensional nanomaterials have weak out-of-plane van der Waals force interactions, resulting in a stacked structure that is easily sheared. In addition, their atoms are tightly connected through in-plane covalent interactions [14,21,22]. This kind of structure provides 2D nanomaterials with distinctive electronic, physical, and chemical properties. These properties include excellent carrier mobility, ultra-high specific surface area, flexibility, thermal conductivity, and optical transparency. The use of atomic force microscopy (AFM)/friction force microscopy (FFM) techniques and simulation software has led to the discovery that many 2D materials are capable of structural superlubricity. Several intrinsic mechanisms have been proposed to explain this phenomenon. The main 2D materials include single-element materials like graphite, graphene, phosphene, tellurene, and graphyne (GDY), as well as 2D transition metal disulfides like MoS_2, WS_2, $MoSe_2$, $NbSe_2$, and other 2D materials like *h*-BN, and MXene, etc. [23].

Therefore, this review explores the surface structural superlubricity properties of major 2D materials, starting with the surface and interlayer friction of 2D materials, delving into the microfriction dynamics between their interlayers and surfaces, and concluding with an outlook on their applications at the macroscopic scale. Section 2, 'Structural Superlubricity Characteristics of 2D Materials', discusses the superlubricity properties of major 2D materials demonstrated in experiments and simulations. Section 3, 'Mechanisms Affecting the Robust Structural Superlubricity', explains the material-intrinsic mechanisms and various tribological externalities that impact structural superlubricity. Section 4, 'Progress in Macroscale Structural Superlubricity', summarizes the current progress and major issues in achieving stable structural superlubricity from a macroscopic perspective. Section 5, 'Summary and Prospects', provides a summary of the previous three sections and presents an outlook for the future realization of robust superlubricity at the macroscale. The outline is shown in Figure 1.

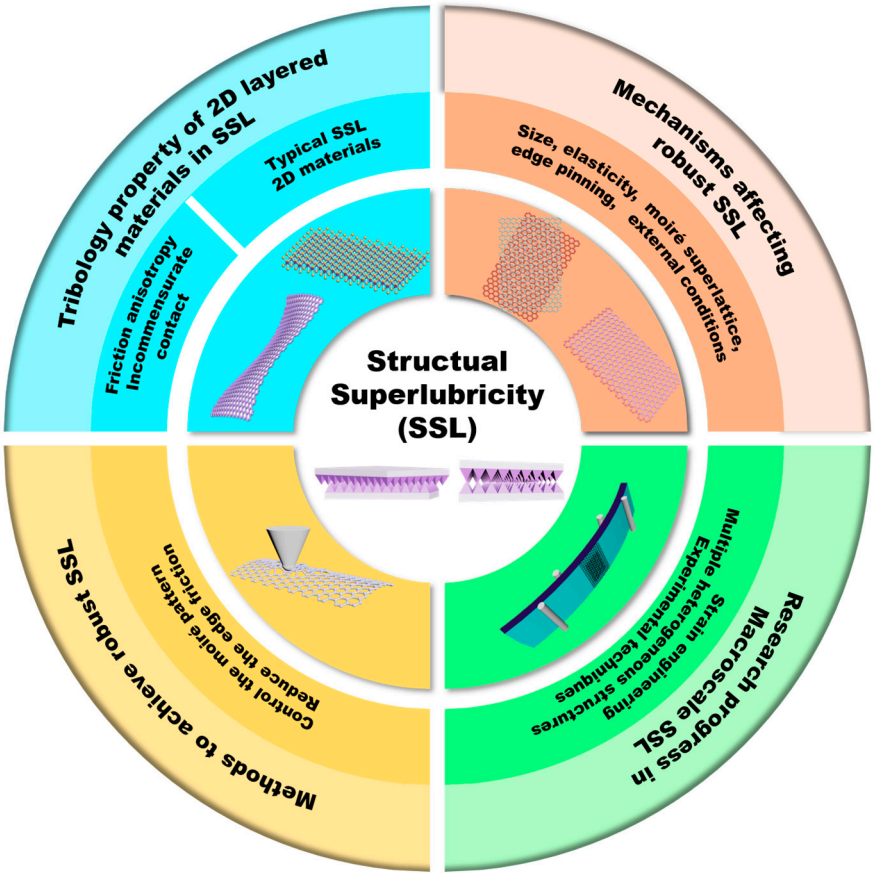

Figure 1. The outline of properties, mechanisms, methods, and research advances that are relevant to structural superlubricity research in 2D materials.

2. Structural Superlubricity Characteristics of 2D Materials

2.1. Incommensurate Contacts and Frictional Anisotropy

To understand the superlubricity properties of 2D materials, it is necessary to probe their tribological behavior and underlying mechanisms to explain the phenomenon through a variety of experiments and simulations [24]. The initial theoretical approach suggested that structural superlubricity requires two rigid crystals with incommensurate structures [5]. The friction contact, which is incommensurable, refers to two surfaces in contact when the surface corrugations do not match or when there is a lattice mismatch. When two crystalline surfaces that are commensurate come into contact and slide against each other, the wave peaks and troughs become embedded in each other (Figure 2b). This causes the frictional contact points in the basal troughs to be on the same side. However, when two incommen-

surate crystalline surfaces slide relative to each other, the frictional contact points in the basal troughs are distributed on both the left and right sides (Figure 2a). This results in lateral friction that cancels each other out, as shown in Figure 2c [25]. In reality, the contact surface properties are much more complicated than the model in Figure 2, which requires a better explanation of the frictional properties of microinterfaces using theories at the atomic and molecular levels [26]. For a single-point contact, the Prandtl-Tomlinson model is generally used [27]. This model describes a point on a contact surface being dragged by a spring with a stiffness coefficient of k in a periodic potential field with period a_0 and amplitude U_0. Stick-slip motion occurs when the dimensionless parameter $\eta = 4\pi U_0 / \left(k a_0^2\right)$ is greater than one, and smooth motion conditions are satisfied when it is less than one [28]. However, when discussing polyatomic and multipoint contacts, it is necessary to explain the interactions between neighboring atoms at the interface using the Frenkel-Kontorova model [29]. Computational simulations, such as molecular dynamics (MD) simulations and the first principles method, have been developed based on these two nanofriction models for tribological applications.

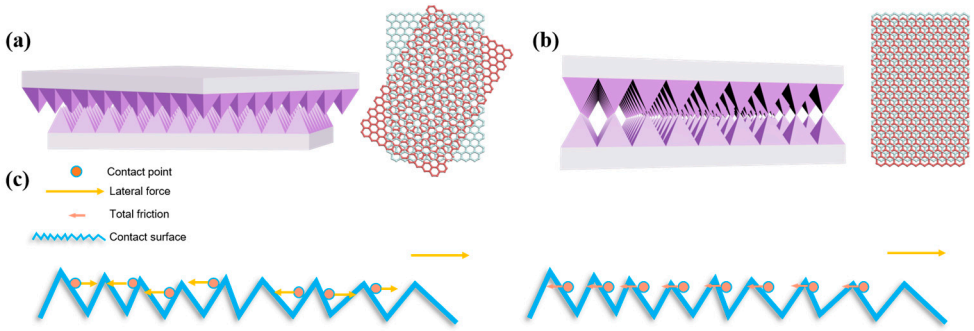

Figure 2. Schematic of two incommensurate contacts to achieve almost zero friction: (**a**) incommensurate contact with the stacking form in 2D materials; (**b**) commensurate contact; (**c**) simple mechanical analysis on zero friction.

Frictional anisotropy is a significant feature observed in materials with structural superlubricity, in addition to incommensurate contact. Frictional anisotropy refers to the phenomenon where the friction force displays anisotropy based on the lattice mismatch between the two friction partners [24,30–32]. Hirano and Shinjo discovered anisotropy in the shear surface friction of single-crystal white mica and single-crystal graphite, which was dependent on the lattice mismatch angle under vacuum drying conditions in 1993 [30]. This study demonstrated that friction is lower in the direction where the degree of incommensurate contact is greater (~30°) for single crystals with a six-fold axis of symmetry. Conversely, friction is higher in the direction of commensurate contact, i.e., in the vicinity of the axis of symmetry. These findings align with the laws derived from the theory of structural superlubricity through the incommensurate contact in twisted 2D layered material flake [33]. Liu et al. have experimentally investigated the tribological properties of graphite-graphite homogeneous contact, specifically focusing on achieving structural superlubricity [34,35]. They were achieved by twisting the graphite flakes in both vacuum and atmospheric environments, changing the stacking angles, and applying lateral load. A lock-in phenomenon was observed when the stacking mode of graphite flake was incommensurate near the six-fold axis of symmetry. In these positions, there is unfavorable relative sliding, high friction, and deformation of the graphite layer, and the friction in the interlayer is almost zero when they slide relative to each other at locations of incommensurate contact, resulting in a self-retracting motion (Figure 3a). AFM shear tests were conducted on highly oriented pyrolytic graphites (HOPGs) at different temperatures and friction vectors were plotted (Figure 3b) [36]. The temperature has an impact on the frictional anisotropy of graphite flakes.

The 2D materials with both homogeneous and heterogeneous structures exhibit frictional anisotropy. A heterostructure exhibits lower friction anisotropy and coefficient of friction (COF) and is more robust in achieving an ultra-low friction state than a homogeneous structure [37,38]. AFM friction tests were conducted to measure the interlayer friction in single-crystal graphite/*h*-BN and demonstrated that the interlayer exhibits sliding anisotropy (Figure 3c) [34,39]. However, the COF near the six-fold axis of symmetry is one order of magnitude higher than the asymmetric directions. Claerbout et al. investigated the frictional anisotropy of MoS_2 through simulations [31]. The MD method is used to simulate the relationship between the sliding direction and tribological behavior of MoS_2 with an initially commensurate structure R180 [32]. The results showed that there is a stick-slip motion in the sliding directions of 0 and 60 degrees. In contrast, the friction of other nonsymmetric directions transitions smoothly with very small values. The direction of least friction is the 30 degree direction (Figure 3d).

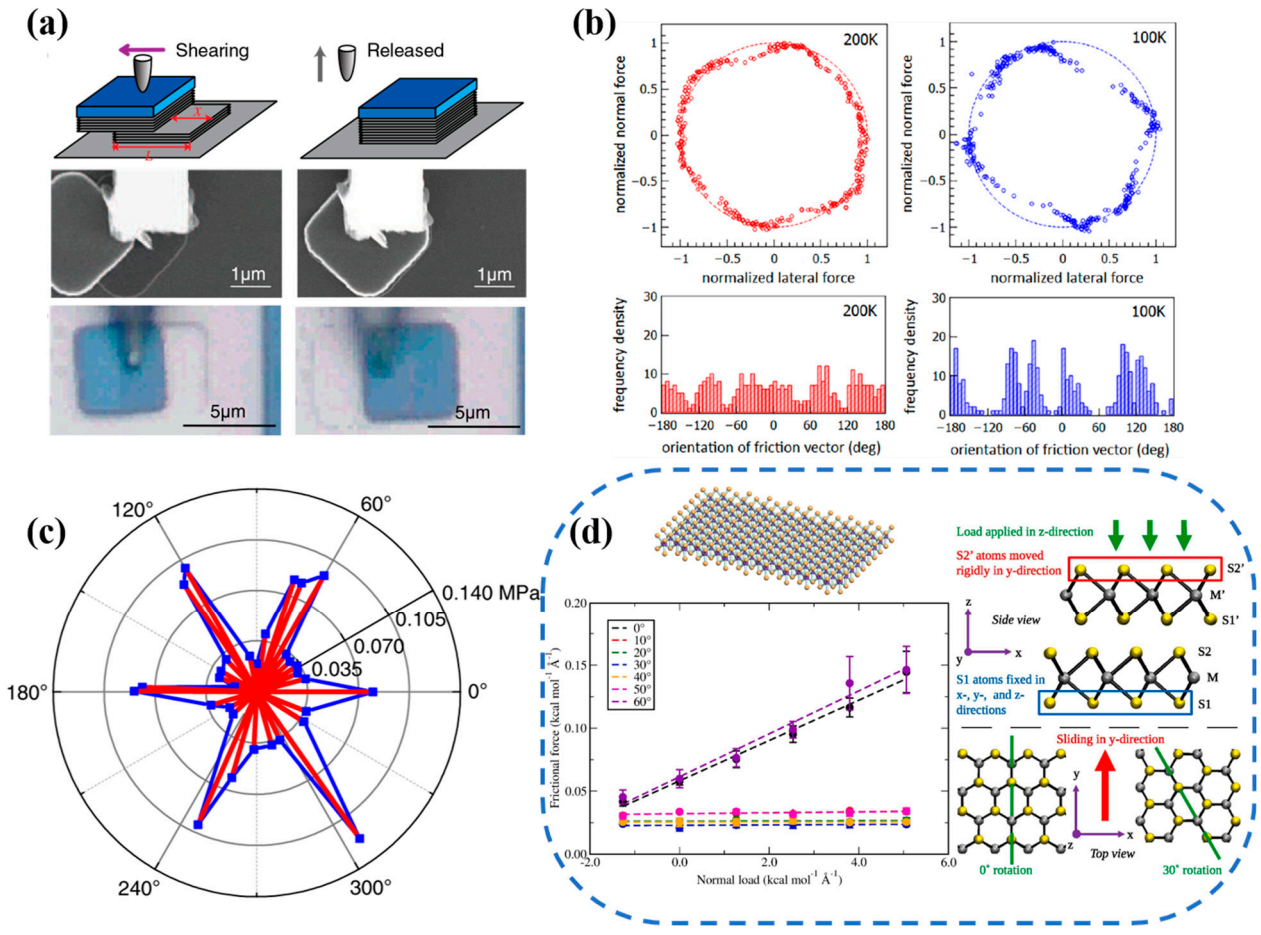

Figure 3. Friction anisotropy affecting structural superlubricity in 2D materials: (**a**) self-retraction motion of the graphene flake. Reprinted from [35], copyright (2012), with permission from American Physical Society. (**b**) Friction vector plots of rotated HOPGs in 200 K and 100 K. Reprinted from [36], copyright (2023), with permission from American Physical Society. (**c**) Schematic diagram of the lateral friction variation with twist angle in graphene/*h*-BN heterostructure. The blue line indicates the change of friction force versus twist angle. Reprinted from [39], copyright (2018), with permission from Springer Nature. (**d**) The interlayer sliding direction anisotropy in commensurate MoS_2. Reprinted from [31], copyright (2019), with permission from Elsevier.

Obviously, frictional anisotropy is a universal property in the tribological behavior of 2D materials. However, recent studies showed that the initial incommensurate contact state of two materials is not a prerequisite for achieving a structural superlubricity [31,40],

the underlying mechanism is that the friction of sliding surfaces is influenced by the stacking sequence of the contact surface at different twist angles and the out-of-plane deformation during sliding. This review provides a detailed analysis on this kind of mechanism in Section 3.

Frictional anisotropy experiments are increasingly used to study the phenomenon of structural superlubricity in materials. By improving twisting dynamics and AFM/FFM experiments to test friction anisotropy and combining them with MD and first-principles simulations, researchers can discover more intrinsic tribological behavioral features [24].

2.2. Single-Element 2D Materials

Single-element 2D materials [23], such as graphite, graphene, graphdiyne, phosphorus, and tellurene, as well as 2D metals like Au, Pt, and Sb, have been shown to achieve superlubricity in both homogeneous and heterostructure forms [41–44]. Graphite and graphene are the most extensively studied 2D materials in the field of structural superlubricity. They are composed of carbon atoms arranged in a hexagonal orientation, stacked layer by layer, with weak interlayer forces. The layer interval is 0.34 nm [45]. The frictional anisotropy between graphite flake layers under vacuum and ambient conditions, as well as the self-retraction motion under superlubricity, was experimentally demonstrated by using the AFM/FFM shear test technique [35,46]. Based on this result, in relative sliding tests by applying a lateral center load, the graphite sheet produced an unstable rotation at the critical displacement (Figure 4b). When an eccentric lateral load was applied, the graphite sheet kept relatively sliding and did not rotate within a short distance until the rotation became unstable at farther critical displacement (Figure 4c) [47]. Additionally, there was a significant difference in friction at the edges of graphene layers. The armchair edges have a minimal impact on the friction of graphene [48], while zigzag edges can produce friction by two orders of magnitude as compared to that on the basal plane [49,50]. Additionally, annealing graphene can significantly reduce friction on zigzag edges [50].

With the breakthroughs of both simulations and experiments, other single-element 2D materials have also proven to have structural superlubricity. Graphyne (GDY) is a 2D carbon allotrope with excellent electronic properties, good chemical stability, and strong mechanical properties. Its special alkyne bonding makes GDY flexible, which improves its fracture toughness [43,51,52]. Ruan et al. investigated the phenomenon of structural superlubricity at the interface of twisted bilayer GDY through simulations [43]. A structural superlubricity is achieved when the twist angle is located within the range of 1 to 59 degrees. Additionally, the size of a superlattice formed at the interface is inversely proportional to the friction coefficient at different twist angles [43]. Monolayer tellurium, a novel 2D material, has been demonstrated to have properties similar to those of 2D layered materials [53]. In addition, heterojunctions formed by metal nanoparticles on the surface of HOPGs also exhibit structural superlubricity [17,54,55]. The frictional behaviors of different groups of gold nanofilms and amorphous antimony nanofilms were evaluated on graphite substrates [17,55]. The results revealed a general scaling law for the frictional force versus the contact area of metal particles with graphite under structural superlubricity. This is explained through the size effect in Section 3. The scaling law of platinum nanoparticles on graphite substrates is not significantly different from that of gold on graphite [54]. However, the overall friction exhibits a greater rate of change with contact area than that of gold [56].

2.3. TMDs

The 2D transition metal dichalcogenides (TMDs) have a compact X-M-X intralayer sandwich structure and weak van der Waals forces between layers, where M is a transition metal atom and X is a sulfur-like atom [23,45,57]. Among them, transition metal dichalcogenides (TMDs) with hexagonal structures (2H phase) exhibit tribological properties similar to graphite and have electronic structures characteristic of semiconductors. TMDs are considered as the second most important materials for structural superlubricity after the graphite family, with many discoveries made in ultra-high vacuum conditions [58].

MoS_2 and WS_2 are commonly used as solid lubricants and are particularly suitable for vacuum applications [45,59]. Like bilayer graphene, bilayer MoS_2 has a hexagonal structure (2H phase) and exhibits frictional anisotropy in the sulfur-rich layer due to grain orientation [21,23,60,61]. However, the interlayer sliding barrier of MoS_2 is higher than that of graphene due to contact area, surface roughness, and strong interlayer atomic interactions compared to graphene, resulting in higher interlayer friction under the same conditions [62]. The rotated structure of bilayer MoS_2 has lower friction and exhibits superlubricity properties [40], in which the shape of the moiré superlattice formed in the rotated structure is the key to achieving structural superlubricity. However, rotation and the generation of lattice mismatch angles are not the only conditions for the realization of superlubricity, which has also been shown to occur in nonrotating commensurate structures in the sliding direction within 0 to 60 degrees [31]. Similar to graphene, MoS_2 also exhibits frictional anisotropy [63]. It has been reported that applying a high tensile strain to the zigzag edge of MoS_2 or a high compressive strain to the armchair edge can greatly reduce edge-dominated friction [64].

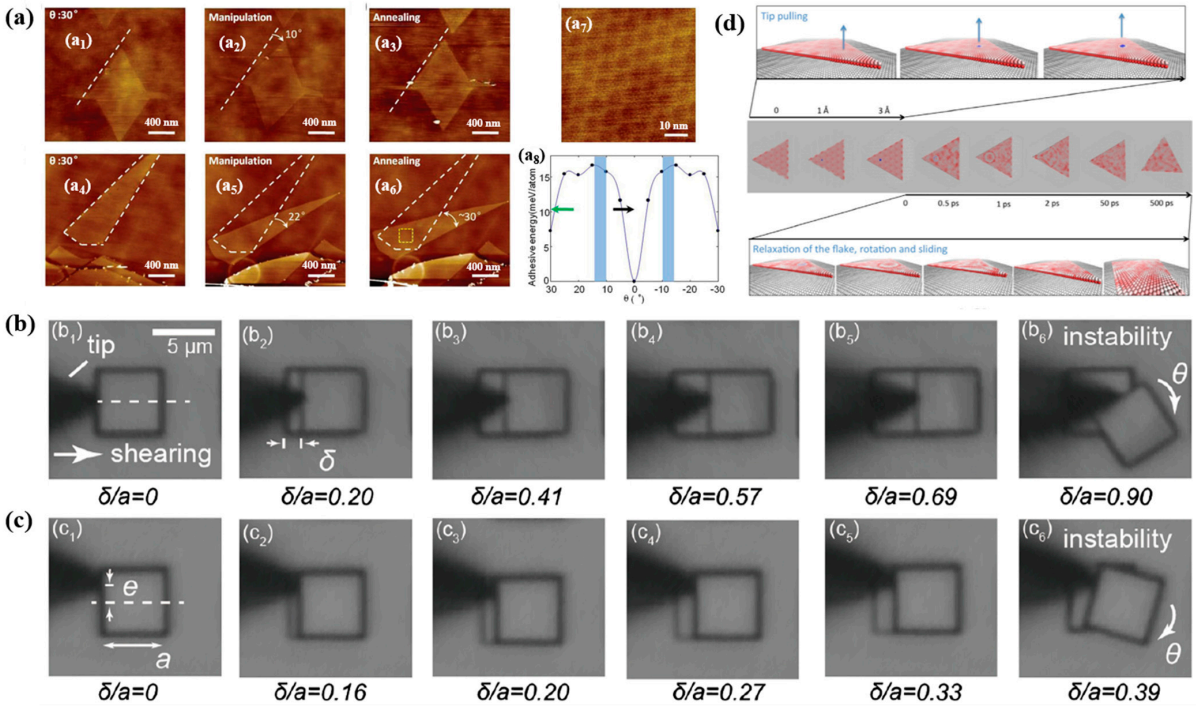

Figure 4. The rotational instability of SSL 2D materials. (**a**) AFM graph about rotational instability of annealing-treated graphene/BN at different twist angles. ($\mathbf{a_1}$–$\mathbf{a_6}$) The edges of the graphene in the as-prepared 30°-twisted G/h-BN samples are marked by dashed white lines, ($\mathbf{a_7}$) represents an enlarged AFM image of the yellow square area depicted in ($\mathbf{a_6}$), ($\mathbf{a_8}$) Bonding energy of the G/h-BN stack as a function of stack angle from first-principles simulations. The blue curve is a fit of the energy. The green arrows (corresponding to $\mathbf{a_1}$,$\mathbf{a_2}$) and the black arrows (corresponding to $\mathbf{a_5}$,$\mathbf{a_6}$) indicate the heat-induced rotational tendencies. Reprinted from [37], copyright (2016), with permission from American Physical Society. (**b**,**c**) Images from the top view on the rotational instability of graphite. ($\mathbf{b_1}$–$\mathbf{b_6}$) The atomic force microscope applies a load near the symmetry axis of the graphite sheet, resulting in the sheets sliding relative to each other. ($\mathbf{c_1}$–$\mathbf{c_6}$) The tip exerts a load at a specific eccentricity *e* from the symmetry axis of the graphite sheet, thereby driving the relative sliding of the graphite sheet**.** Reprinted from [47], copyright (2019), with permission from American Physical Society. (**d**) Rotational instability of graphene/WS_2. Reprinted from [65], copyright (2018), with permission from Springer Nature.

In addition to MoS_2, other TMDs have been studied for their structural superlubricity. The impact of superlattice-induced lattice distortion on structural superlubricity at

$MoS_2/MoSe_2$ heterojunction interfaces was investigated using first-principles calculations [66]. The forbidden bandwidth is closely related to the layer-layer twist angle. If the band gaps of the two materials have a large difference, the sliding energy barrier will be lower for the material with the narrower band gap. On the other hand, if the band gaps of the two materials are relatively close, the sliding potential barrier will be smaller for a smaller moiré superlattice size. The superlubricity behavior of a monolayer of WS_2 in epitaxial graphene on a SiC substrate was investigated via scanning probe microscopy (SPM) tip triggering [65]. The WS_2 overcomes sliding barriers to undergo rotational and translational motions on the epitaxial graphene, eventually rotating to rest in the direction of 60° symmetry at the graphene interface (Figure 4d), which displays a similar characteristic of rotational instability as that of graphite flakes [47]. However, the WS_2 sheet does not generate any strain and there is no formation of moiré superlattice at the interface. These observations suggested that WS_2 has a weak interaction with graphene [65]. The above studies provide valuable insights into the regulation of structural superlubricity by homogeneous or heterogeneous structures constructed by other TMD families.

2.4. h-BN-Based 2D Materials

h-BN, also referred to as white graphite, is composed of atomically flat layers made up of alternating hexagonal B and N atoms. Its structure is composed of a network of BN_3 rings that are stacked in layers, and the interlayer interaction forces are typically stronger than those in laminated graphite and MoS_2 [45,67]. However, due to its hexagonal layered structure, good thermal stability, and its strong resistance to oxidation, it has become an excellent lubricant. Furthermore, numerous experiments and simulations demonstrated that *h*-BN presents several novel discoveries associated with superlubricity. A rotating bilayer *h*-BN that overcomes the rotational energy barriers is demonstrated to be superlubric, exhibiting lower friction but lower stability compared to the nonrotating unit, using a density generalized function model of the interlayer sliding potential energy surface [40]. However, the homogeneous structure formed by the *h*-BN bilayer must overcome rotational resistance. If its twist dynamics are not regulated, it will spontaneously revert to a commensurate high-friction state [40]. Therefore, an increasing number of experiments and simulations have shown that *h*-BN-based heterostructures can exhibit more robust superlubricity in various rotational states. Heterostructures of sufficiently large graphene and *h*-BN have natural lattice mismatches that allow robust superlubricity when other external conditions are ignored. However, frictional anisotropy remains almost unchanged [34,68]. The structural potential energy of the graphite and *h*-BN heterojunction increases monotonically as the twist angle increases from 0 to 30 degrees [69]. The friction between graphene and *h*-BN follows a stick-slip mechanism based on MD simulations [27]. The stick-slip motion is affected by the strong coupling of in-plane and out-of-plane deformation induced by moiré superlattice at different twist angles. Furthermore, rotational instability was also observed to be similar to that of graphite flakes when testing the friction behavior of a graphene/*h*-BN heterojunction through high-temperature annealing [37]. The annealing process controls effectively the rotational behavior and moiré superlattice structure of the heterojunction interface (Figure 4a). A moiré superlattice with smaller wavelengths can be achieved by using higher annealing temperatures, longer times, and smaller graphene sheets on *h*-BN. Additionally, graphene tends to rotate towards 0° or 30° depending on whether the twist angle is below or above the critical angle θ_c, which is approximately $12 \pm 2°$.

In summary, many 2D materials exhibit similar superlubricity properties, which are caused by incommensurate contact or sliding in an asymmetric direction with frictional anisotropy. With scientific and technological progress, both advanced friction testing techniques and simulation methods are increasingly being used to study structural superlubricity. On the experimental side, for example, the rotational resistance in the relative sliding of graphite flakes was measured using the 'push-edge' and 'drag-center' methods [69] and the morphological structure of graphite contact surfaces after sliding was

better characterized using the flip-and-pick (pick-flip technique) [70]. MD simulations and first-principles calculations were used to analyze a series of interlayer frictional dissipation mechanisms. These mechanisms include moiré superlattice-induced atomic-level interlayer shape structure [71,72], interlayer sliding potential energy surface (PES) fluctuation differences [72], and twisting dynamics [73] in 2D materials. The scope of research on structural superlubricity was gradually expanded to include ambient conditions [74–76], pointing to the future realization of structural superlubricity at the macroscale. In addition, structural superlubricity in 2D materials is typically influenced by various factors, including the stacking of these two materials, the angle of lattice mismatch resulting from the rotation of surface layer, out-of-plane and in-plane deformation, environmental conditions, and kinetic friction dissipation mechanisms at the edges, which are analyzed in the following section. The research on surface superlubricity of 2D materials is being extended to cover instability to stability, from the microscale to the macroscale, and from the ideal to the real environment, by the current need for research on structural superlubricity.

3. Mechanisms Affecting the Robust Structural Superlubricity

3.1. Methods of Microdynamic Simulation

The calculation of kinetic simulations is essential to investigate frictional dissipation mechanisms in structural superlubricity at the microscale. The most commonly used computational methods are MD and first-principles calculations based on density functional theory (DFT).

Molecular dynamics (MD) simulation is widely used to study tribological properties of surfaces and interfaces at the nanoscale [77,78]. This method employs Newton's second law to determine the movement of atoms. Atomic forces are calculated from the gradient of the total potential. The choice of materials depends on compatible empirical potentials. For instance, the second-generation reactive empirical bond order (REBO) potential [79], which is based on solid carbon and hydrocarbon, is commonly utilized to represent atomic interactions on graphite surfaces; the interlayer interactions of layered materials, including graphene, can be described using the Lennard-Jones (L-J) potential [80], but this empirical potential greatly underestimates the frictional properties of layered materials. Additionally, the MD database includes other empirical potentials, such as the Kolmogorov-Crespi (K-C) potential [81,82] and the embedded atom method (EAM) [83]. The MD calculation software like LAMMPS [43,81,84] contains many empirical potentials and important parameters such as temperature, contact area, load, and velocity. To ensure computational accuracy in MD, several correction potentials have been developed based on classical empirical potentials. For example, the L-J potential can be corrected using the complementary Gaussian potential [85]. However, graphene and other 2D materials have complex potentials and a large number of degrees of freedom. This complexity can reduce the accuracy of classical MD simulations. To address this issue, a smoothed molecular dynamics theory (SMD) with a much larger time step size (one order of magnitude larger than MD) was then proposed by Wang et al. [86]. Using the MD-SMD method based on symplectic load balancing, they simulated the classical structural superlubricity friction analytical model, which yielded good accuracy and efficiency. However, the classical MD method is less accurate than the density functional method (DFT) due to heavy reliance on empirical potentials [40].

The tribological behavior of material surfaces can be studied through potential energy surfaces (PES) in a given system using DFT-based first-principles calculations [87,88]. The position of each atom on the PES is optimized for minimum energy. The computed PES can be used as input to classical models in nanotribology, such as the P-T and F-K models, or to test empirical potentials used in classical mechanical models. Understanding fluctuations in PES is often crucial for analyzing and interpreting interlayer friction anisotropy and energy states [89]. During the analysis of the contact surface edges, DFT-based calculations can be used to determine the presence of chemical bonding between the sliding layer and the substrate [84].

3.2. Size and Layer Effect

The superlubricity of 2D material surfaces is primarily affected by size, including contact area and layer thickness. As the contact area increases, the number of dislocation motions on the surface also increases. Therefore, the elastic-plastic deformation cannot be neglected. As a result, the rigid model cannot be used to analyze superlubricity at large contact sizes [33]. Once the contact area surpasses a certain threshold, the superlubric state ceases to exist. Despite this, some researchers continue to explore the potential of structural superlubricity for use in larger contact sizes.

For instance, in the case of graphite, various techniques have been developed to investigate the superlubric properties of its structures at different scales, ranging from nanoscale probes testing surface sliding of nanographene to coating-coated tips examining surface friction of micron-scale multilayer graphene [90], and even tips pushing large-size graphite sheets for relative sliding on graphite surfaces [91] (Figure 5a) [49]. Furthermore, the sublinear relationship between contact area and friction was applied to achieve structural superlubricity quantification in related studies [17,55,92,93]. Dietzel et al. demonstrated that friction under structural superlubricity is dependent on a sublinear relationship with the contact area [55]. Herein, a scale was introduced to be related to the out-of-plane deformation and frictional anisotropy, expressed as $F \propto F_0 A^{\gamma}$. γ is the lattice mismatch angle orientation related to frictional anisotropy, also known as the structural superlubricity characteristic factor. It has a value of 0 or 0.5 for perfectly rigid crystals or amorphous bodies [94]. When $0 < \gamma < 0.5$, the friction variation rule concerning the size of crystals on the substrate surface meets the condition of structural superlubricity (Figure 5b,c) [55]. Yan et al. expanded on this by adding variates related to the twist angle and the shape of the moiré superlattice to the original scale law [93]. In addition to the scaling laws, the critical size is also a crucial factor that affects structural superlubricity. A more generalized scaling law was proposed to clarify the relationship between friction and contact area from sublinear to linear for systems larger than 1 μm, which is affected by interior-controlled friction (red area), otherwise, the sublinear relationship is influenced by rim-controlled friction (blue area) as shown in Figure 5d [95]. In this case, the unit of the frictional action is no longer per atom, but per moiré superlattice. The law follows as $\frac{F}{F_0} \propto \sigma A + A^{\frac{1}{2}} + A^{\gamma}$, unlike Dietzel's proposed scaling law. Moreover, the sliding of metallic antimony particles on MoS_2 surfaces was also investigated by Dietzel et al. [62]. As the contact size between MoS_2 and antimony increases, there is an abrupt change in the ratio of static to kinetic friction around a critical size in contact area of 20,000 nm^2, which results in a nearly five-fold increase in relative sliding difficulty (Figure 5e). According to the results obtained by Qu et al. [49], the total friction is mainly due to atomic interactions at the edges for contact sizes smaller than ~10 μm, and due to in-plane atomic interactions for contact diameters larger than 10 μm. At the microscale, the shape of moiré superlattice varies between layers of 2D materials with the size of the contact area [96]. Specifically, there are multiple critical values for the ratio of contact size D to moiré period L_m.

In addition to contact size, the nanotribological properties of four 2D materials, namely graphene, MoS_2, $NbSe_2$, and *h*-BN, on a silica substrate were investigated to evaluate the effect of layer thickness on friction [97]. It is worth noting that the friction decreases as the number of layers increases, which may be due to the increased sensitivity of thin layers to external elastic deformation. Additionally, the surface stiffness of 2D material sheets depends on the sheet thickness (Figure 5f). However, this tendency is suppressed when the substrate adheres more strongly to the sheet. A recent study explains the relationship between the number of layers and friction in 2D materials [98]. At lower loads, the relationship between the number of layers in 2D materials and friction is not always consistent with the commonly accepted rule that more layers result in a lower friction. The magnitude of friction is not solely determined by the number of layers, but also by the coupled effects from the plastic deformation of the substrate, the wrinkles on the surface of the topmost layer, and other factors [98].

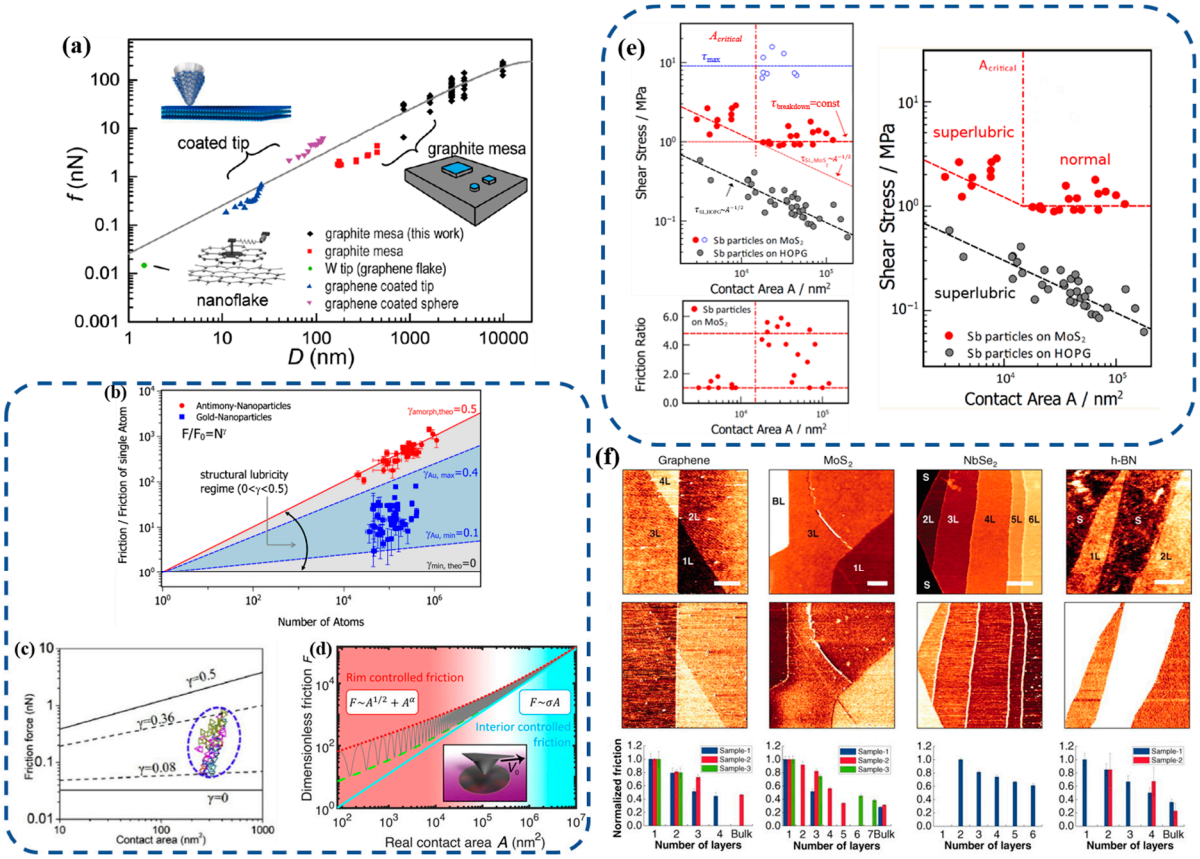

Figure 5. Friction versus contact size and layered thickness among van der Waals materials. (**a**) Friction test strategies about SSL graphite and graphene that are relevant to contact size. Reprinted from [49], copyright (2020), with permission from American Physical Society. (**b**–**d**) are scaling laws concerning friction with the change of size in metal nanoparticles/graphite, Au/graphite, and graphite/*h*-BN heterointerfaces. The black arrow in (**b**) and the blue circle in (**c**) represent the scope of the structural superlubricity. Reprinted from [55,92,95], copyright (2013, 2020, 2019), with permission from American Physical Society, Elsevier, American Chemical Society. (**e**) Surface friction versus contact size of MoS_2. Reprinted from [62], copyright (2017), with permission from American Chemical Society. (**f**) Relationship between friction and the number of layers. Reprinted from [97], copyright (2010), with permission from The American Association for the Advancement of Science.

3.3. Elasticity Effect

The microscopic nature of self-retraction motion observed in 2D materials like graphite was explored, and the elastic deformation of the sliding interface becomes more pronounced with increasing contact size. A finite element method based on the continuum medium model was utilized to analyze the interlayer deformation and in-plane deformation of twisted graphene sheets on a rigid graphene substrate [99]. The potential energy in the small-angle large-size elastically twisted bilayer graphene (tBLG) interlayer was significantly reduced by elastic structural relaxation and localized strains. This revealed the competing relationship between the elastic strain energy and the tBLG interlayer potential (Figure 6a). The elastic effect was a result of the principle that local lattice mismatch caused a change in the stacking of interlayer atoms, leading to the formation of local AB-stacked (commensurate) domains and AA-stacked domains. When the layers slid relative to each other, shear strain was generated along the boundary between the two domain walls, forming a localized strain soliton, which is also called saddle point (SP) stacking [81,99,100]. An elastic model for MD simulations was utilized to examine the impact of surface elasticity on the superlubricity phenomenon of multilayer graphite flakes in contact with a graphite substrate of 120 nm × 120 nm [81]. The results obtained via this method were an order of

magnitude lower compared to the friction calculated under the rigid model. The in-plane elastic deformation of incommensurate surface contacts can be neglected [49].

In conclusion, the elastic effect is closely related to the size and shape of the material. It is most significant on the contact surface of materials stacked with large contact sizes and small twist angles, which have lower interlayer potential energy. Additionally, 2D materials in commensurate and large contact exhibit strong elastic effects [101]. The elastic deformation results in the localized formation of stable AB stacking domains and unstable AA stacking domains. A strain is generated between two domain walls and forms a linear SP region with unstable AA stacking domains connected at both ends. Interestingly, this region, formed by AA-AB-SP, is a moiré superlattice with one period.

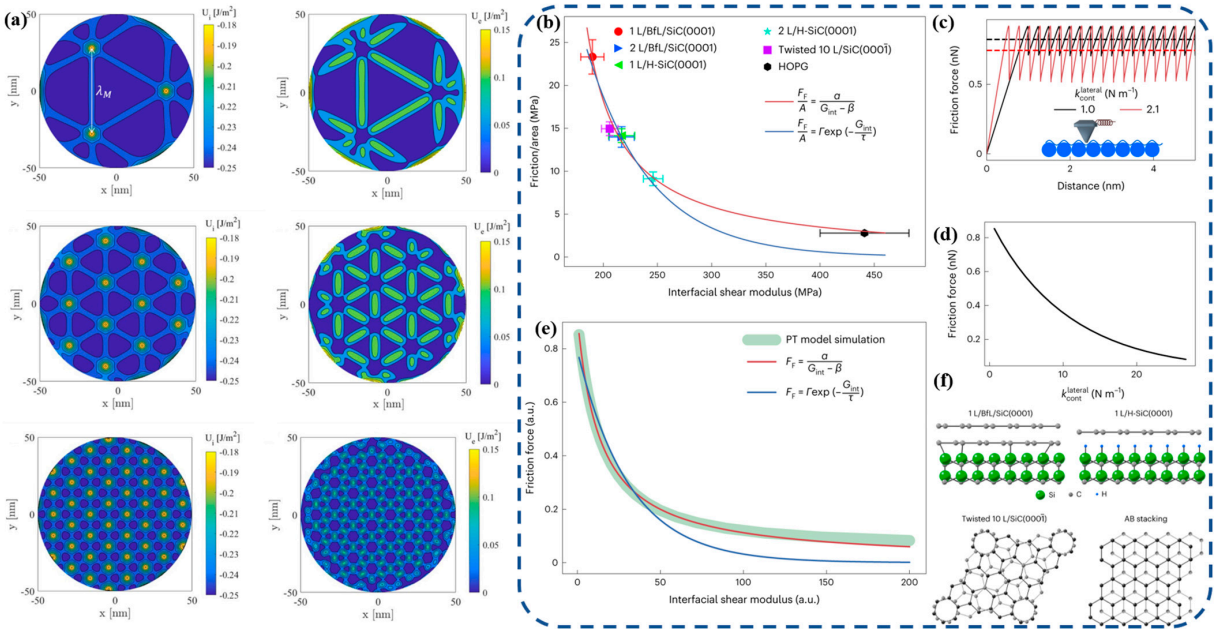

Figure 6. The elasticity-related parameters of twisted graphene homogeneous structure. (**a**) interlayered potential energy (**left**) and elastic strain energy in twisted bilayer graphene (**right**). (**b**) Friction per unit contact area as a function of interlayer shear modulus; (**c**) the curve of friction with tip sliding distance in the P-T model. The inset shows the schematic of the P-T model; (**d**) the relationship between friction and contact lateral stiffness $k_{cont}^{lateral}$ calculated from the P-T model; (**e**) the simulated function about friction versus interfacial shear modulus fitted by a two-parameter exponential decay function and two-parameter reciprocal function; (**f**) atomic model schematics of epitaxial graphene layer/buffer layer/SiC (0001) (labeled as 1 L/BfL/SiC (0001)), 1 L/H-SiC (0001), Twisted 10 L/SiC (0001) and commensurate AB stacking. (**a**) Reprinted from [99], copyright (2022), with permission from Elsevier. (**b**–**f**) Reprinted from [102], copyright (2022), with permission from Springer Nature.

In addition, the sliding friction is closely related to the shear modulus of different materials [102,103]. It has been demonstrated that the critical contact size maintaining an ultra-low friction state depends on the shear modulus of the material [103,104]. The sliding friction of twisted graphene on a pyrolytic graphite substrate was measured in consideration of only two important parameters of shear elastic modulus and shear force [102]. Noteworthily, there is an inversely proportional relationship between shear modulus and friction force (Figure 6b–e). It is inferred that there is a general inverse relationship between shear elastic modulus and friction for other 2D materials on SiC substrates. Additionally, a mechanism for superlubric friction dissipation of 2D materials in a superlubric state is proposed, which involves low shear modulus-to-potential amplitude-to-lateral deformation and increased energy dissipation.

3.4. Moiré Superlattice

In 2D materials with incommensurate contact under structural superlubricity, a moiré superlattice pattern is often observed, significantly altering the properties of materials. For instance, the surface of the so-called 'magic corner graphene' exhibits excellent optoelectronic properties controlled by the moiré superlattice pattern [105]. As explained in the previous section, a moiré cell is a polygonal region consisting of AA-AB-SP. The shape of the moiré superlattice is dependent on the stacking arrangement of the two 2D materials. Related studies demonstrated that robust structural superlubricity can be achieved by regulating the size of the moiré superlattice between layers of 2D materials [44,96,106,107].

The relationship between elastic strain energy and interlayer potential energy through the shape of the moiré superlattice was investigated by Morovati et al. [99]. Specifically, the length of the moiré stripes indicates the magnitude of elastic strain energy, while the size of AA-stacked domains versus AB-stacked domains within the moiré cell reflects the magnitude of the interlayer potential energy [99]. The shape of the moiré superlattice between bilayer graphene layers is quantitatively characterized by constructing a statistical method for lattice mismatch intervals [96]. The method identifies the superlubricity versus nonsuperlubric states by using histograms. The shape of the moiré pattern under superlubricity shows a normal distribution (Figure 7(a_3)). Based on this, how the persistence of moiré superlattice shape-induced superlubricity is affected by the twist angle and contact size was investigated, noteworthily, a critical twist angle of 1.5° and a critical ratio of the contact size D to moiré period (the length of the strain soliton) [100]; L_m, are required for robust superlubricity (Figure 7(a_1,a_2)) [96]. The tribological behavior of a multilayer graphene moiré superlattice was further investigated by considering the effect of elastic deformation on the moiré superlattice shape-induced superlubricity [108]. Thicker 2D materials with smaller out-of-plane deformations and stronger interlaminar interactions reduce corresponding moiré superlattice periods, resulting in a lower friction and a higher sliding stability (Figure 7b). The correlation between moiré superlattice and friction on rotating bilayer graphdiyne surfaces was reported by Ruan et al. [43].

Besides graphene, other 2D materials follow the same law between friction and moiré superlattice, and the friction coefficient decreases when increasing the size of the moiré superlattice formed on the rotating GDY surface. This is due to the decrease in interlayer charge transfer, potential energy corrugation, and fluctuations in the average charge density at the interface during sliding (Figure 7c). Bao et al. investigated the moiré superlattice changes in bilayer α-phosphene, bilayer β-phosphene, and α-phosphene/β-phosphene heterojunctions in relative sliding [44]. The moiré superlattice of bilayer β-phosphene consistently exhibits a hexagonal structure. In contrast, the moiré superlattice of bilayer α-phosphene transforms from a tetragonal shape to a one-dimensional linear shape as the twist angle increases. Additionally, the α-P/β-P heterostructures always maintain the shape of linear stripes, as shown in Figure 7d. In addition, a load-independent, low-anisotropic, ultra-low friction structure was achieved by simulating the moiré superlattice structure between MoS_2 and Au (111) substrate with a Si tip in the opposite direction [109]. The moiré superlattice structure was controlled with a twist angle of 4.5° and a moiré period of about 3.3 nm by a single-atom epitaxial MoS_2 structure on the Au (111) surface under ultra-vacuum conditions.

In summary, the shape of the moiré superlattice is determined by the coupled effects of elastic strain energy from out-of-plane deformation and the interlayer potential energy generated during stacking [44,99]. The amount of out-of-plane deformation is determined by the shear modulus, while the interlayer potential energy is influenced by the stacking of 2D materials. Additionally, the surface structure of 2D materials is determined by parameters such as twist angle and contact area. Therefore, the study of moiré superlattice provides a new method to achieve robust structural superlubricity. This can be accomplished by selecting 2D materials with a large shear modulus and regulating the shape of the moiré superlattice on their surfaces. This will result in appropriate interlayer potential

energy and elastic strain energy of out-of-plane deformation, ultimately leading to robust superlubricity. This is crucial for the development of sustainable superlubricity technology.

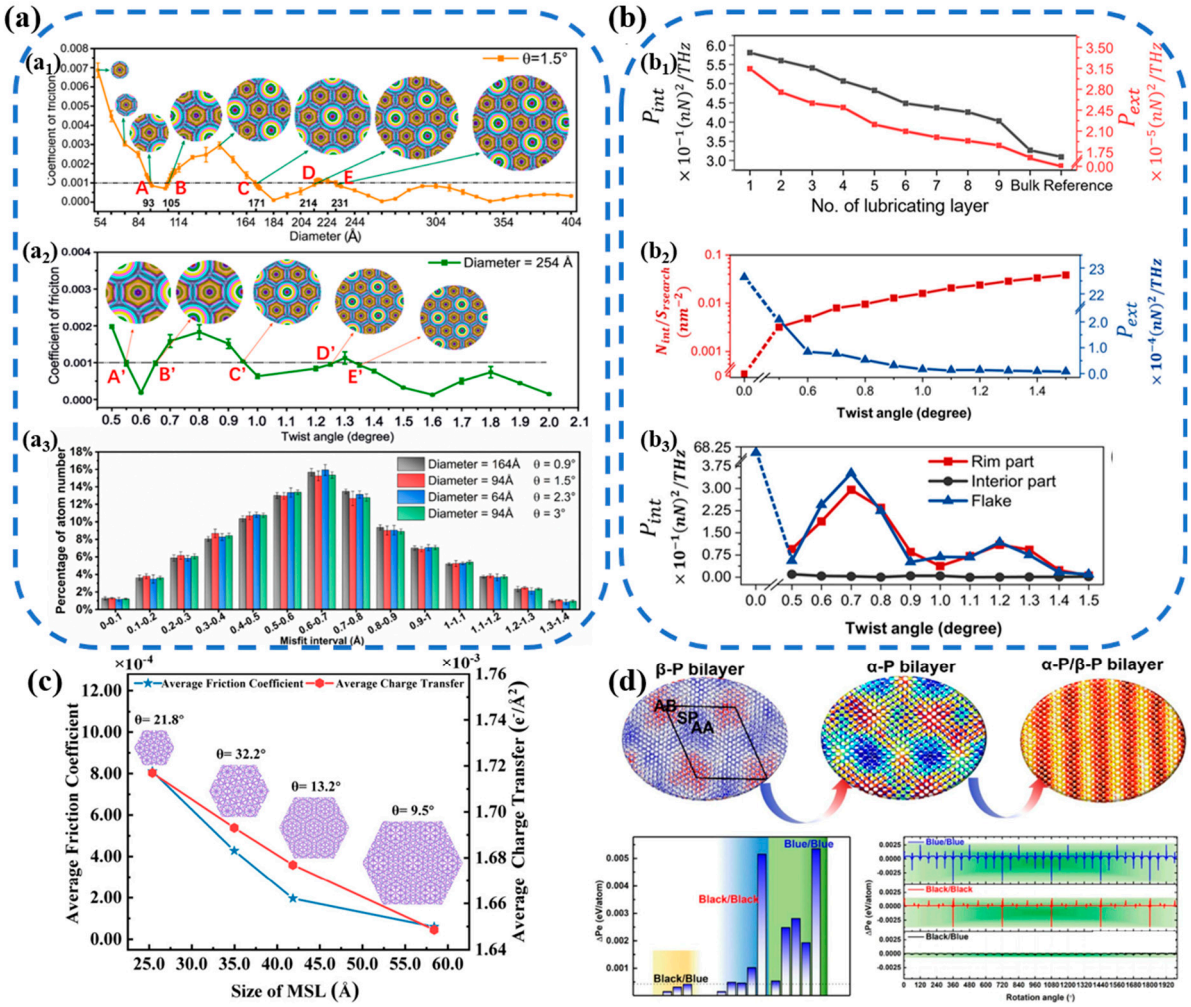

Figure 7. The mechanism that affects the moiré pattern by twist angle (lattice mismatch) to achieve superlubricity. (**a**) Frictional behavior in tBLG and the distribution of atoms in per misfit interval that reflects different moiré superlattice's shapes. (**a**$_1$,**a**$_2$) show the coefficient of friction as a function of graphene sheet diameter for a twist angle equal to 1.5° and a fixed diameter of 254 Å respectively. (**a**$_3$) The time-averaged proportions of atoms per mismatch interval for a series of graphene flakes in the superlubricated state. Reprinted from [96], copyright (2022), with permission from Elsevier. (**b**) Inter and external friction power curve versus number of layers (**b**$_1$) and twist angles (**b**$_2$,**b**$_3$). Reprinted from [108], copyright (2023), with permission from American Chemical Society. (**c**) Frictional behavior of twisted bilayer graphdiyne by controlling the angle to change the size of moiré superlattice (MSL). Reprinted from [43], copyright (2021), with permission from American Chemical Society. (**d**) The moiré pattern affecting frictional behavior of 2D homogeneous and heterogeneous phosphorene. Reprinted from [44], copyright (2022), with permission from Elsevier.

3.5. Edge Effect

Generally, the total friction between layers and surfaces of layered 2D materials is composed of internal friction and edge friction. In 2D materials with small sizes, the friction is mainly caused by the edges [49,84,95,110]. Especially for heterogeneous structures, the contribution of edge atoms to friction is one to two orders of magnitude larger than that of in-plane atoms [111].

The edges of 2D hexagonal materials exhibit significant frictional anisotropy, where relative sliding along the zigzag edge has a higher friction than along the armchair edge. This

phenomenon is particularly pronounced in hexagonal structures [49,50,64]. Furthermore, the high activity of the edge atoms makes them prone to defect formation and interaction with external matters, or atoms in the low potential barrier region of the substrate. For instance, the zigzag edges of graphene can readily interact with atoms of F and H, resulting in the formation of edge dimers [55,93,111,112]. The frictional behavior of graphene edges was investigated to evaluate the role of edge atoms by using ab initio calculations [110]. Out-of-plane deformation profiles were obtained for two types of edges (dimer edges and pristine edges) at twist angles of 0 and 90 degrees. Noteworthily, there was almost no edge-pinning effect under commensurate contact (0°). However, under incommensurate contact (90°), the out-of-plane deformation of the dimer edge was significantly higher than that of the interior. Additionally, the out-of-plane deformation of the pristine edge, which did not form a dimer, was very small (Figure 8a,b).

In addition to graphene, using the contact surface of MoS_2/*h*-BN as an example, the coordination number of S atoms near the edges is lower than that of the internal S atoms. This results in weak chemical bonding of the edge S atoms, making them more prone to run into the minimum potential energy region of the *h*-BN substrate. Therefore, a pinning effect of the upper edge on the substrate is generated [84]. As a result of MD calculations, it was found that the root-mean-square displacements (RMSDs) and sliding potentials of the edge atoms were larger than those of the inner atoms (Figure 8c). In addition to the edges of layered materials, the steps on substrates also produced edge-pinning effects. For instance, in the case of graphene substrate steps, two types of step edges were found: 'exposed step' and 'buried step' [113]. The pinning effect at the step edge is attributed to the interaction between free chemical bonds of the sliding layer and the substrate [84,113]. If there is no chemical interaction at the sliding interface, the resistance to rise can be completely canceled by the descending momentum. However, if there is a chemical interaction, the resistance to rise is significantly greater than the descending momentum, resulting in higher friction. The exposed steps of graphene are chemically distinct from the basal plane, making them more susceptible to chemical interactions and edge-pinning effects. For instance, OH^- is found at the end of the exposed step edges and is prone to hydrogen bonding interactions with the surface [114].

Therefore, the factors that cause the edge-pinning effect can be summarized as the interaction between the chemical bonds of the sliding layer edge and the free chemical bonds of the substrate. Sliding layer edges that are composed of unsaturated bonds are more susceptible to pinning than those composed of saturated bonds. Furthermore, the greater the number of exposed steps on the substrate surface, the higher the probability of chemical interactions with the surrounding substrate atoms, resulting in a stronger step-edge pinning effect [113].

To reduce the edge pinning effect, it was necessary to decrease the interaction between the chemical bonds of the sliding layer edge and the free chemical bonds of the substrate. MoS_2/Cu_2O composite films were synthesized via liquid-phase synthesis, in which MoS_2 film edges were pinned on 40 nm Cu_2O nanospheres [115]. The composite film exhibited macrosuperlubricity on carbon steel, with a friction coefficient of only 0.006 (see Figure 9a–d). When applying concentrated stress at the center of the graphene and Si surfaces, the load was lower than what was required to maintain the superlubric state of the structure [75]. As a result, the bending moments generated at the edges overcame the van der Waals forces between the layers, causing the edges of the graphene surfaces to warp (Figure 9e–h). Additionally, the friction coefficients of the interface between graphite flake and nanostructured silicon were measured at various loading positions. These positions were determined by the eccentric distance, δ, between the loading position and the center of the flake, as illustrated in Figure 9i. By analyzing the histograms of warping height versus eccentricity δ (Figure 9j) and the curves of surface friction versus normal force at different load application positions (Figure 9k), it was concluded that the edge warping disappeared when the eccentricity reached a certain value, resulting in a significant increase in friction

with increasing the normal force, which demonstrated the crucial role of edge warping in reducing edge friction.

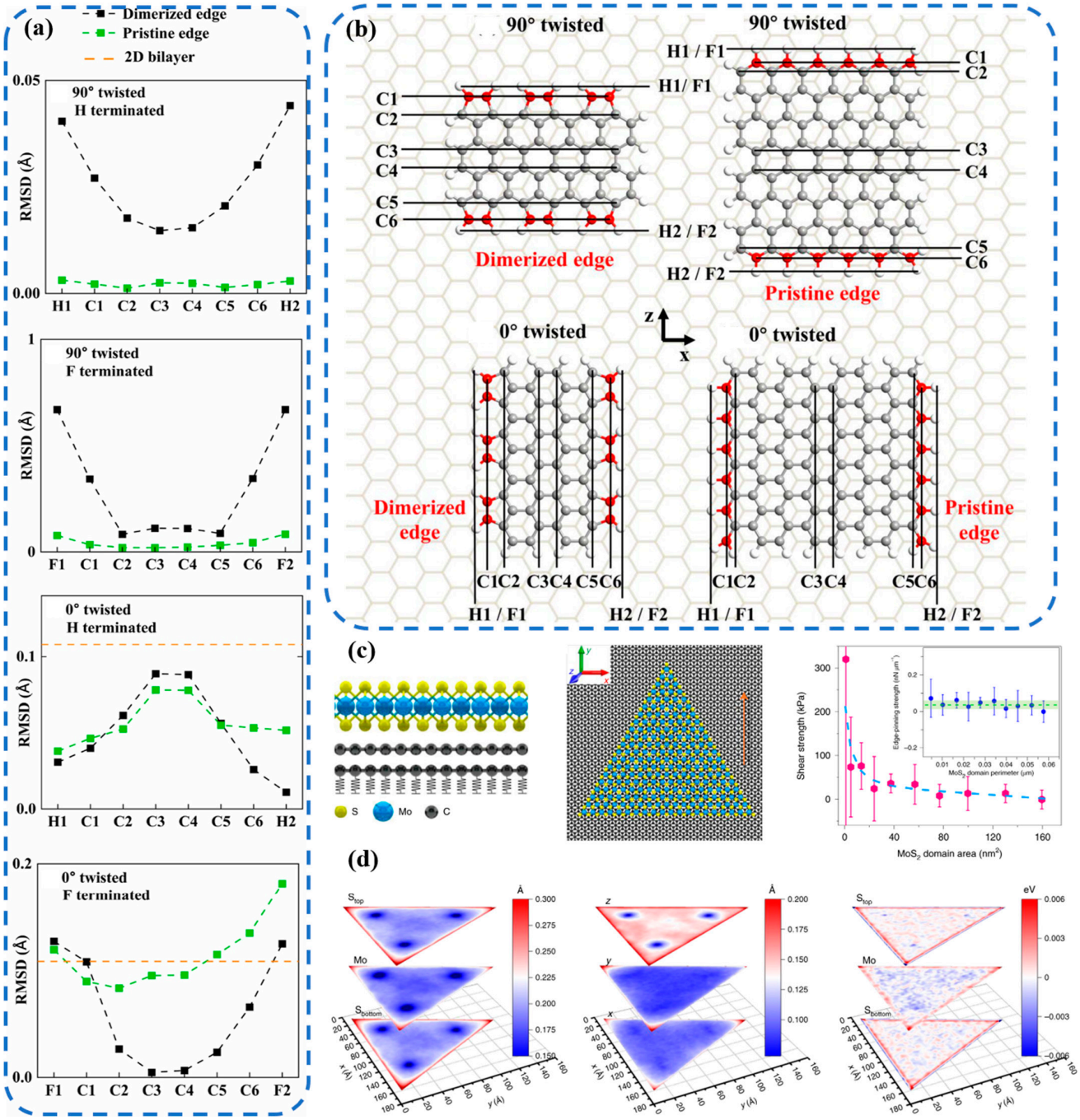

Figure 8. The mechanism of edge-pinning effect in tBLG and bilayer MoS_2. (**a**) The root-mean-square displacements (RMSDs) curve following the sliding path of edge-to-interface to the edge. (**b**) The different rows that represent internal atoms, H terminated edge and F terminated edge are defined by C1, C2, C3, C4, C5, C6, and H1/F1, respectively. (**c**) MD results of MoS_2 sliding on the graphene. The illustrations depict the side view (left) and top view (middle) of the computing device. The blue dash line (right) in the inset shows the calculated edge pinning strength as a function of the perimeter of MoS_2 flakes. (**d**) The mappings of the RMSDs of atoms (left and middle) and potentials (right) concerning the equilibrium positions of different atomic layers of MoS_2. Reprinted from [84,110], copyright (2023, 2021), with permission from Elsevier and Springer Nature.

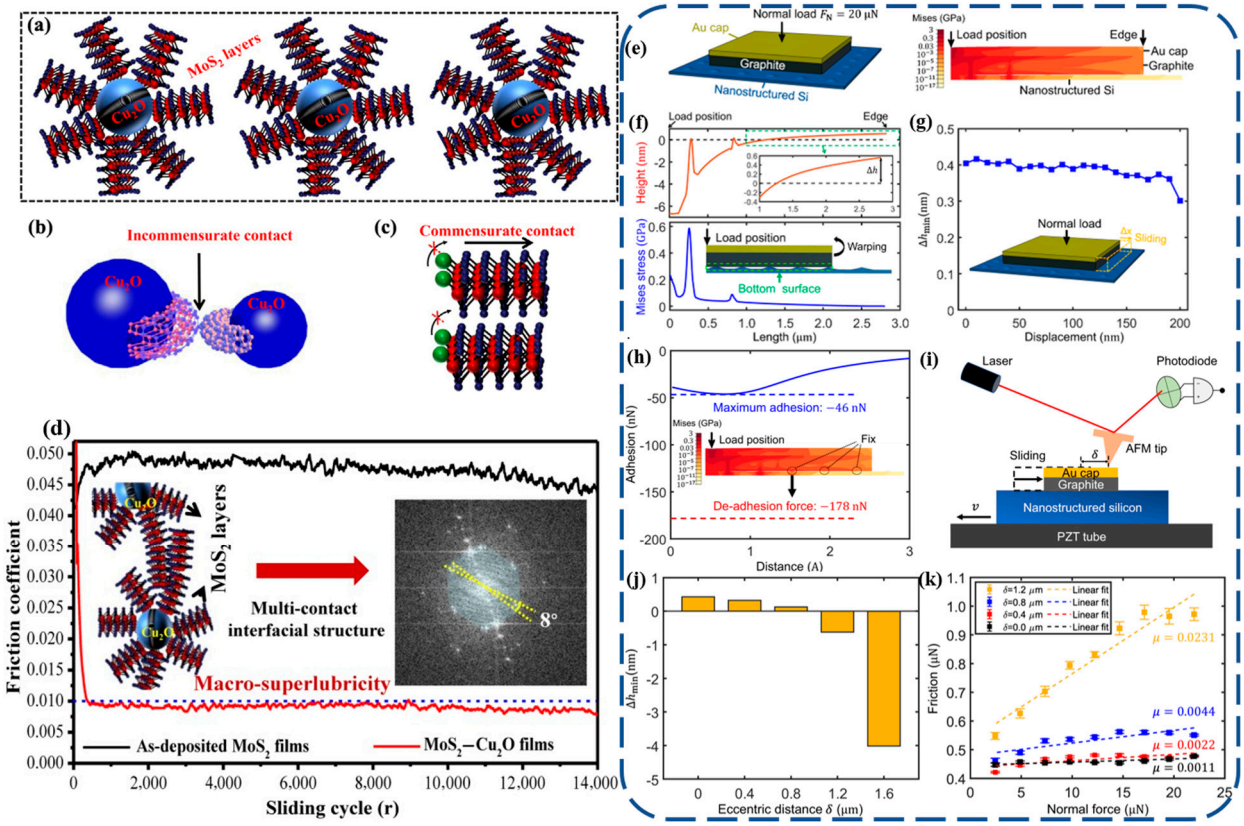

Figure 9. Methods for suppressing edge friction. (**a**–**d**) Complex of MoS_2 edge atoms with Cu_2O. Reprinted from [115], copyright (2023), with permission from Springer Nature. (**e**–**k**) Applying centrally concentrated loads to graphite flakes in a graphite flake-graphite device. Reprinted from [75], copyright (2023), with permission from Springer Nature.

Therefore, there are two main categories of solutions to the edge pinning effect: edge modification with lower energy-saturated chemical bonds, or modulation by external conditions, such as the application of concentrated stress loads to warp the edges and prevent contact with the substrate surface. Other schemes, such as appropriately increasing surface roughness during material design, may reduce the edge-pinning effect [75]. However, further experimental studies are necessary to confirm this point.

3.6. External Conditions

In addition to the material itself, the stability of structural superlubricity can be affected by conditions such as load, sliding velocity, and temperature. Liu et al. utilized a platinum (111) surface to cultivate graphene monolayers [107]. The variations of friction with normal load were simulated by using MD simulations for two surfaces with different sizes of moiré superlattices, R2 (L_{R2} = 2.2 nm) and R30 (L_{R30} = 0.5 nm) (see Figure 10a–e). Different frictional dissipation mechanisms were revealed at lower and higher loads, and only at higher loads (F_n > 40 nN), the regulation of moiré superlattice size had a greater effect on friction. The friction on graphene/Pt (111) surfaces due to moiré superlattice and normal load was dependent on the sliding velocity [116]. However, first-principle calculations have shown that friction decreases with increasing load under certain conditions [117]. Recent research has demonstrated that the relationship between load and friction is dependent on the presence or absence of an interfacial layer formation at the contact surface. This formation is related to atomic diffusion [118]. When the sliding velocity is below a certain critical value, the effect of moiré superlattice size and normal load on friction is almost negligible. However, above a critical velocity, the friction varies exponentially with sliding velocity, and it can be regulated by changing the moiré superlattice size and normal load

(Figure 10f,g). Wang et al. investigated the temperature dependence of sliding friction in twisted graphene [22]. The frictional dissipation mechanism is related to moiré superlattice fluctuations and reaches a saturation constant when the temperature is below T_c (blue region). On the other hand, when the temperature is above T_c (red region), the frictional dissipation is related to major thermal bending fluctuations (Figure 10h) [22]. Using the Te/graphene heterostructure obtained by Ru et al. [41] as an example, the variations of friction with load, temperature, and sliding velocity are investigated by modulating the moiré superlattice with α-Te/graphene, β-Te/graphene, and α-Te/β-Te rotating sliding layers (Figure 10i). The variations of friction with load, temperature, and sliding velocity on the α-Te/graphene surface is the least affected by external conditions such as load. Robust superlubricity can be achieved independently of external conditions by selecting an appropriate structure.

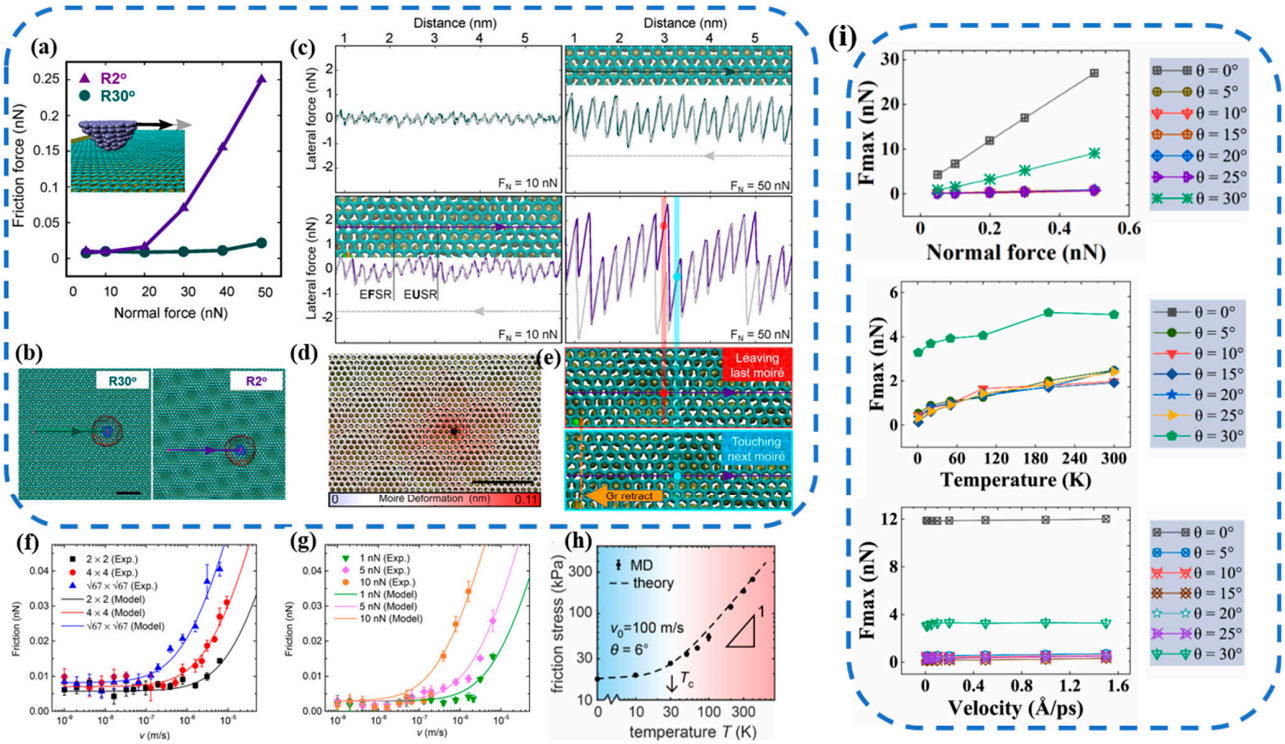

Figure 10. The external factors, such as normal force (**a**–**e**), velocity (**f**,**g**), and temperature (**h**) that affect the moiré pattern to change the friction behavior in typical 2D materials; (**i**) the external factors in α-tellurene/graphene. Reprinted from [22,41,107,116], copyright (2023, 2021,2023, 2022), with permission from American Chemical Society, and Elsevier.

Moreover, a kinetic model was developed for twisted bilayer graphene from a statistical perspective [106]:

$$f\Delta v = m\eta\left(2a_m\Delta z\frac{v_m}{a\Delta x}\right)^2, \quad (1)$$

where a_m is the moiré period, m is the mass of the thin top layer of graphene, Δz and Δx are the amplitude and maximum half-width of the out-of-plane deformation, respectively, which are related to the material properties and the normal load. η is the dissipation coefficient, and v is the sliding velocity. Surfaces with contaminants can also achieve superlubricity. Surface contaminants can create localized incommensurate contacts on the graphene surface, which facilitates the realization of structural superlubricity to some extent [119].

In summary, the stability of superlubricity in 2D material structures is significantly affected by external conditions such as load, temperature, and sliding velocity when they reach respective critical values. A brief summary is presented in Table 1.Therefore, selecting

appropriate materials and regulating the surface structure is quite necessary to enhance the stability of superlubricity under external conditions. This can be achieved by choosing heterostructures with high stiffness, light mass, and small-size moiré superlattices.

Table 1. The summary of mechanisms and factors affecting structural superlubricity and corresponding methods.

Factors	Mechanisms	Methods to Sustain Robust Superlubricity
Size Effects	scaling law/generalized scaling law [55,95]	the scaling law should remain sublinear ($0 < \gamma < 0.5$) [55]
Elasticity Effects	localized strain soliton [81,99,100] Stiffness affecting superlubricity [102]	select 2D materials with high stiffness [102]
Moiré Superlattice	different sizes and shapes control friction [96]	control the shape by twisting and applying strain [44,96,106,107]
Edge Effect (contact size $D < 10$ μm)	interactions among edge atoms [84,113,114]	edge modification, or modulation by external conditions [114,115]
Normal Load	superlubric state (The formation of sublayers) [118] nonsuperlubric state (critical load F_c without sublayers) [107]	control variables to obtain the most stable parameters for superlubricity [106,107,116].
Sliding Velocity	friction increases as speed and load increase (up to V_c) [116]	
Temperature	moiré fluctuations ($<T_c$) and thermal bending fluctuations ($>T_c$) [22]	

4. Progress in Macroscale Structural Superlubricity

In recent years, researchers have pursued the goal of achieving robust structural superlubricity at macroscopic scales. However, there are currently two major challenges facing the applications of macrorobust superlubricity. Firstly, the structural superlubricity of 2D materials is greatly affected by ambient conditions. Secondly, it is difficult to achieve superlubricity for 2D materials with large sizes. However, it was concluded from the analysis in the previous section that constructing suitable heterostructures of 2D materials and modulating the moiré superlattice on the surface of the structure can achieve structural superlubricity independent of environmental conditions to a large extent. That is a significant advance toward the commercialization of structural superlubricity for future technologies like MEMS, frictionless mobile connectors, hard disk drives, and mechanical bearings that operate in extreme environments [25].

AFM-based transverse manipulation experiments about gold islands on graphite under ambient conditions were conducted in 2016 [56]. The atomic contact area between the gold island and the graphite substrate ranges from approximately 4000 to 130,000 nm^2. The results indicated that the friction during sliding was extremely low, less than 2.5 nN. In 2017, a study demonstrated that macrosuperlubricity was achieved on graphene-based surface structures by preparing millimeter-scale multilayer graphene coatings wrapped with microspherical probe. The coefficient of friction is of the order of 10^{-3} in ambient air with a load of 1.45 μN, which can keep robust superlubricity in the air up to 51% RH [90]. The principle behind this technique involves the presence of numerous bumps on the surface of microspheres coated with 2D materials. Each bump makes random contact with the surface, resulting in incommensurate contact overall. Furthermore, this arrangement disperses the positive loads applied to the surface, significantly enhancing its load-carrying capacity. Based on this principle, Zhang et al. designed a friction test system consisting of a millimeter-scale graphene-coated plate (GCP), graphene-coated microspheres (GCS), and graphene-coated balls (GCB). The system was based on the design of coated-encapsulated microspheres, as shown in the inset in Figure 11a [120].

The GCB/GCS/GCP system achieves stable superlubricity, with a coefficient of friction of 0.006, after running for 1200 s at a sliding velocity of 0.2 mm/s in air at 35 mN. Based on the multicontact graphite microsphere technology, the layer-by-layer ordered sliding structure design for each single contact point has achieved robust macroscale superlubricity performance on rough and laser-weaving steels [121]. The coefficients of friction are 0.007 and 0.006, respectively. Androulidakis et al. applied strain to randomly stacked graphene surfaces prepared via mechanical exfoliation and CVD [122]. The maximum frictional interlaminar shear stress (ILSS) value for millimeter-scale surfaces under ambient conditions was estimated to be 0.13 MPa, achieving macroscale superlubricity (Figure 11b). The susceptibility to shear on the macroscale in bilayer graphene is thought to be caused by the presence of random incommensurate stacking, wrinkles, and lattice mismatch induced by differences in tensile strain. Wang et al. demonstrated how strain engineering can achieve macrosuperlubricity, which is to alter the shape of the moiré superlattice on the material surface under strain [123].

Furthermore, an increasing number of experiments have combined multiple techniques to achieve macrorobust superlubricity on larger scales. Li et al. designed a contact load dispersed strained graphene/MoS_2/fullerene-like carbon hydride (FL-C: H) ternary composite system (Figure 11c) [124]. The deformation is applied to a highly elastic FL-C: H substrate to disperse the load concentrated on graphene/MoS_2. Graphene with fewer defects is prepared using the vacuum ball-shearing exfoliated graphene (BSEG) technique, which reduces interaction with environments and improves environmental stability. Finally, the heterostructured system of graphene/MoS_2 is achieved through incommensurate contact and regulated moiré superlattice at the surface for optimal superlubricity. Ultimately, the designed system achieves robust macroscale superlubricity with a coefficient of friction (COF) of 0.007 under a forward load of up to 15 N and a relative humidity (RH) of 20%. In addition, Yang et al. transformed multiple nanoheterojunctions into homogeneous structures by doping graphene edges with oxygen, which effectively suppresses the edge effect. The structure exhibits ultra-low friction (with a COF of approximately 0.005) across a wide range of loads, speeds, and temperatures (from −200 to 300 °C) [125].

In summary, three main approaches have been demonstrated to be capable of achieving macroscale structural superlubricity: (1) strain engineering on the surface of 2D materials [64,122,126] to disperse concentrated stresses and modulate the surface shape; (2) preparing microsphere probes covered by coatings of 2D materials to combine multiple microscale superlubricity through multiple contact points [90,120,121]; and (3) considering combinations of multiple techniques to prepare heterostructure composite systems with wider ranges and better macroscale superlubricity [124]. A brief summary is presented in Table 2. In addition, several other schemes have been reported to offer technical and ideological guidance for achieving macroscale robust superlubricity. However, experimental and simulation proofs are still lacking. Recently, it has been discovered that the incorporation of 3D printing and bionic technologies into the structural design of surfaces can achieve ultra-low friction in ambient conditions. For instance, inkjet printing DLP technology can be used to replicate a fish's hook-and-spine cylindrical structure, or the lollipop and 'Y'-shaped gecko foot-like structure, which enables macroscopic lubrication in wet environments and water [127,128]. Zhao et al. utilized a 3D-printed bionic topology coupled with a heterostructure to introduce a MoS_2/$MoSe_2$ heterojunction into a 3D-printed honeycomb round-core square/hexagonal topology of Al_2O_3 [129]. The structure with 30% areal density achieves a stable ultra-low friction coefficient of 0.09 and a low wear rate of 2.5×10^{-5} mm^3 N^{-1} m^{-1} at 5 N (Figure 11d). A very desirable friction coefficient of 0.08 is maintained for 370 s even under a 10 N load, however, it still falls short of the 10^{-3} order of magnitude required for superlubricity.

Table 2. The summary of methods to achieving macrorobust structural superlubricity.

Methods	Examples	Relevant Performance
strain engineering in surface materials	epitaxial bilayered graphene [122]	ILSS: 0.13 MPa [122]
combination of multiple microcontact points	GCP/GCS/GCB composite system [120]	COF: 0.006 [120]
strain + multiple contact points + heterostructure	graphene/MoS_2/fullerene-like carbon hydride (FL-C: H) ternary composite systems [124]	COF: 0.007 [124]

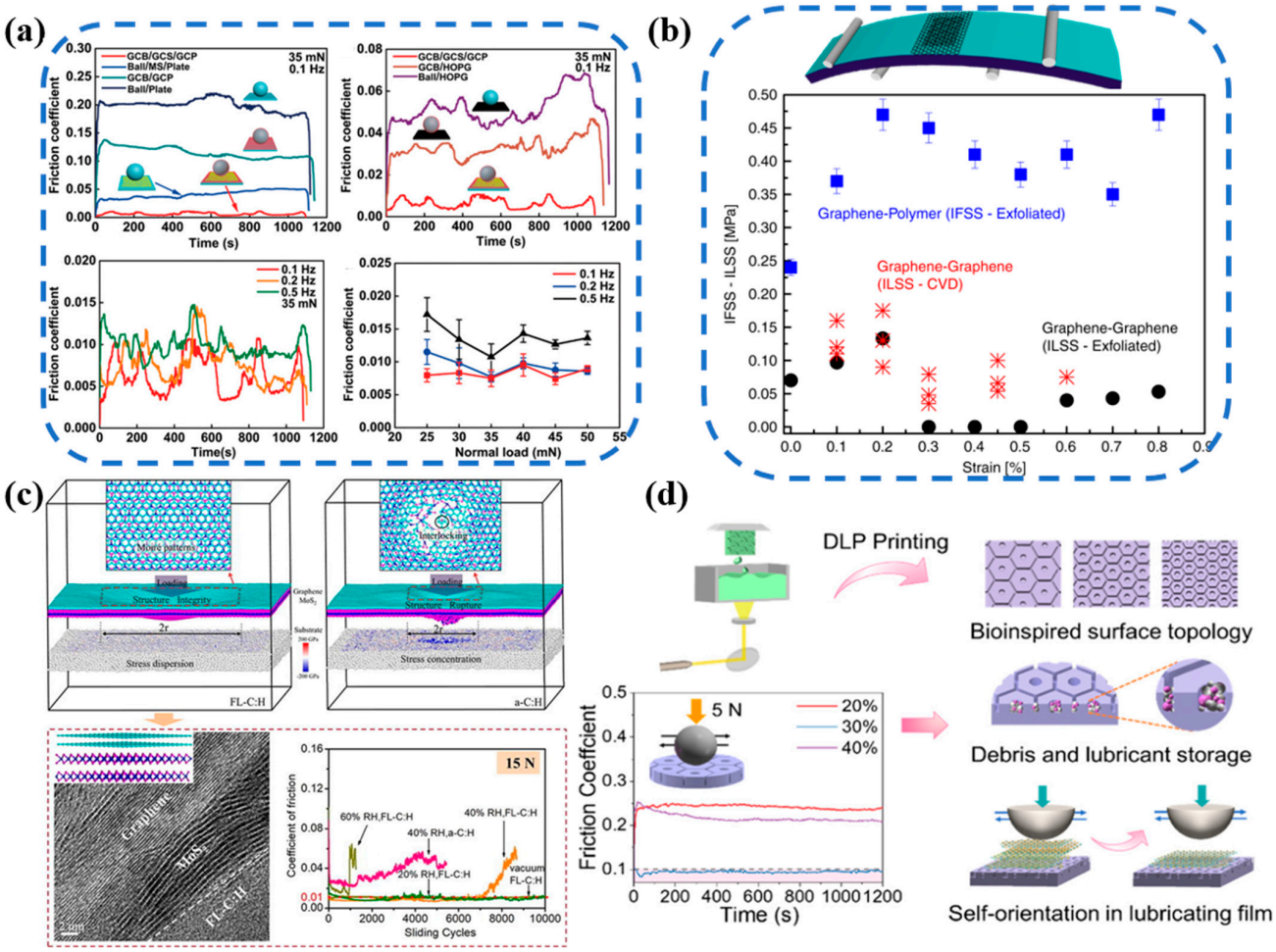

Figure 11. The main methods to achieve macrostructural superlubricity. (**a**) Graphene or other heterostructure-covered microspheres with multiple contact points, Reprinted from [120], copyright (2020), with permission from John Wiley and Sons. (**b**) The strain engineering in bilayer graphene. Reprinted from [122], copyright (2020), with permission from Springer Nature. (**c**) Composite of multiple materials to form heterojunction. Reprinted from [124], copyright (2022), with permission from Elsevier. (**d**) The design of 3D printing structures to store lubricants and form incommensurate contact. Reprinted from [129], copyright (2021), with permission from American Chemical Society.

Furthermore, other programs have not yet established a theoretical system and lack experimental demonstrations, such as the coupling of 3D printing technology with heterogeneous structure preparation. It is expected that the issues hindering the achievement of macrorobust structural superlubricity will be resolved soon. This will enable the application

of structural superlubricity to a wider range of equipment systems. Additionally, as the mechanisms of structural superlubricity continue to develop on larger scales, it presents numerous possibilities for enhancing the service performance and structural stability of various macroscopic devices. For instance, in the machinery industry, it can enhance the friction and wear resistance, as well as the service life of engines, turbines, gears, bearings, and other structural components [12,130]. In medicine, it can improve the precision and efficiency of medical-surgical systems and biodetection systems, as well as enhancing the performance of artificial joints and organs [12,131]. In aerospace and space exploration, it can improve the structural stability of related devices under extreme conditions [21,25].

5. Summary and Prospects

In this paper, starting from the definition of structural superlubricity, which is the friction between two incommensurate contact interfaces close to zero, the structural superlubricity of 2D layered materials was taken as an example, and the characteristics of structural superlubricity of typical 2D materials and the microscopic mechanisms affecting the stability of structural superlubricity were analyzed and summarized in detail from the shallow to the deep. The influences of size effect, elasticity effect, moiré superlattice, edge effect, and external conditions on structural superlubricity of 2D materials were emphasized; there is a strong connection between these factors. In the state of structural superlubricity, there is a sublinear relationship between friction and contact area, however, there is an inverse relationship with the thickness of 2D materials within a certain range. The microtribological behavior in structural superlubricity of 2D materials is essentially the coupled results of elastic deformation and interlayer potential energy, and the shape of different moiré superlattices reflects whether robust superlubricity can be realized. Under the critical contact sizes, the total friction is mainly contributed by the friction of edges, and the source of the edge friction is essentially the interaction of the edge active atoms with the environment and the substrate. In the superlubricity state, the friction is significantly affected by the external conditions especially when the external conditions such as sliding speed, temperature, and so on, reach a certain critical value. Environmental stability can be enhanced by choosing a suitable surface structure and twisting mismatch angles to control the moiré superlattice size.

Finally, this review summarized the research progress in achieving macrorobust superlubricity. Three feasible schemes that have been verified via experiments and simulations are discussed:

1. Applying strain to a 2D material enhances its load-bearing capacity, modulates the shape of its moiré superlattice, and improves its environmental stability.
2. Designing microsphere-shaped friction test probes coated with a 2D material enables the substrate to be covered with a coating or microspheres made from 2D materials. The objective was to achieve numerous point contacts, dividing the whole into a multitude of microscale contacts, which significantly increases the size of materials used for structural superlubricity, and achieves a span from nanometers to millimeters.
3. Combination of various mechanisms and technologies. Preparation of 2D materials with fewer defects and higher stiffness with disproportionate contact conditions. Twisting and applying strain to regulate the moiré superlattice on the surface can minimize surface friction while enhancing environmental stability. Finally, edge friction should be suppressed by methods such as edge modification.

Author Contributions: Conceptualization, F.-B.W. and J.-H.O.; validation, F.-B.W., S.-J.Z. and J.-H.O.; investigation, F.-B.W. and L.C.; resources, F.-B.W., S.-J.Z. and S.-Q.W.; data curation, F.-B.W., S.-Q.W. and L.C.; writing—original draft preparation, F.-B.W.; writing—review and editing, J.-H.O. and L.C.; visualization, F.-B.W. and S.-Q.W.; supervision, J.-H.O.; funding acquisition, J.-H.O. All authors have read and agreed to the published version of the manuscript.

Funding: This work was financially supported in part by the National Major Science and Technology Project, grant number 2021YFB3701405.

Data Availability Statement: Not applicable.

Conflicts of Interest: The authors declare no conflicts of interest.

Abbreviation

MEMS	microelectromechanical systems
TMDs	transition metal dichalcogenides
AFM	atomic force microscopy
FFM	friction force microscopy
GDY	graphyne
MD	molecular dynamics
HOPGs	highly oriented pyrolytic graphites
COF	coefficient of friction
SPM	scanning probe microscopy
PES	potential energy surface
DFT	density functional theory
REBO	reactive empirical bond order
EAM	embedded atom method
SMD	smoothed molecular dynamics
tBLG	twisted bilayer graphene
SP	saddle point
1L/BfL/SiC (0001)	epitaxial graphene layer/buffer layer/SiC (0001)
RMSDs	root-mean-square displacements
GCP	graphene-coated plate
GCS	graphene-coated microspheres
GCB	graphene-coated balls
ILSS	interlaminar shear stress
FL-C: H	fullerene-like carbon hydride
BSEG	ball-shearing exfoliated graphene
RH	relative humidity
English and Greek Alphabet	
k	stiffness coefficient
a_0	period
U_0	amplitude
η	dimensionless parameter for identifying stick-slip motion
θ_c	critical angle
γ	lattice mismatch angle orientation related to frictional anisotropy
σ	friction stress in the moiré tile area
D	contact size
L_m	the minimum moiré period
δ	the eccentric distance
L_{R2}	moiré period with a 2° twist angle
L_{R30}	moiré period with a 30° twist angle
a_m	moiré period
m	mass of the top thin layer of graphene
Δz	amplitude of the out-of-plane deformation
Δx	the maximum half-width of the out-of-plane deformation
η	dissipation coefficient
v	sliding velocity

References

1. Han, T.; Zhang, S.; Zhang, C. Unlocking the Secrets behind Liquid Superlubricity: A State-of-the-Art Review on Phenomena and Mechanisms. *Friction* **2022**, *10*, 1137–1165. [CrossRef]
2. Holmberg, K.; Erdemir, A. Influence of Tribology on Global Energy Consumption, Costs and Emissions. *Friction* **2017**, *5*, 263–284. [CrossRef]
3. Zheng, Z.; Guo, Z.; Liu, W.; Luo, J. Low Friction of Superslippery and Superlubricity: A Review. *Friction* **2023**, *11*, 1121–1137. [CrossRef]

4. Liu, H.; Yang, B.; Wang, C.; Han, Y.; Liu, D. The Mechanisms and Applications of Friction Energy Dissipation. *Friction* **2023**, *11*, 839–864. [CrossRef]
5. Shinjo, K. Dynamics of Friction: Superlubric State. *Surf. Sci.* **1993**, *283*, 473–478. [CrossRef]
6. Lin, J.; Zhang, C.; Liao, N.; Zhang, M. A DFT Analysis on the Superlubricity Performance of Structural Superlubricity Micro/Nano-Component on Silicon-Based Surface. *Tribol. Int.* **2023**, *189*, 109005. [CrossRef]
7. Luo, J.; Liu, M.; Ma, L. Origin of Friction and the New Frictionless Technology—Superlubricity: Advancements and Future Outlook. *Nano Energy* **2021**, *86*, 106092. [CrossRef]
8. Khan, Z.H.; Kermany, A.R.; Öchsner, A.; Iacopi, F. Mechanical and Electromechanical Properties of Graphene and Their Potential Application in MEMS. *J. Phys. Appl. Phys.* **2017**, *50*, 053003. [CrossRef]
9. Yu, Q.; Chen, X.; Zhang, C.; Luo, J. Influence Factors on Mechanisms of Superlubricity in DLC Films: A Review. *Front. Mech. Eng.* **2020**, *6*, 65. [CrossRef]
10. Wang, Y.; Deng, W.; Chen, X.; Qi, W.; Zhang, C.; Zhang, C.; Luo, J. The Effect of Roughness Level of α-C: H Films on Its Tribological Behaviors Rubbing against Steel and Self-Mated Materials. *Tribol. Int.* **2023**, *187*, 108754. [CrossRef]
11. Yang, X.; Wang, Y.; Zhang, J. Scaling up to Macroscale Superlubricity of Sp^2-Dominated Structural Carbon Films: Graphene and Carbon Onion. *Appl. Surf. Sci.* **2023**, *636*, 157784. [CrossRef]
12. Zeng, Q.; Zhang, W. A Systematic Review of the Recent Advances in Superlubricity Research. *Coatings* **2023**, *13*, 1989. [CrossRef]
13. Luo, J.; Zhou, X. Superlubricitive Engineering—Future Industry Nearly Getting Rid of Wear and Frictional Energy Consumption. *Friction* **2020**, *8*, 643–665. [CrossRef]
14. Wang, H.; Liu, Y. Superlubricity Achieved with Two-Dimensional Nano-Additives to Liquid Lubricants. *Friction* **2020**, *8*, 1007–1024. [CrossRef]
15. Peyrard, M.; Aubry, S. Critical Behaviour at the Transition by Breaking of Analyticity in the Discrete Frenkel-Kontorova Model. *J. Phys. C Solid State Phys.* **1983**, *16*, 1593. [CrossRef]
16. Müser, M.H. Structural Lubricity: Role of Dimension and Symmetry. *Europhys. Lett.* **2004**, *66*, 97. [CrossRef]
17. Dietzel, D.; Schwarz, U.D.; Schirmeisen, A. Nanotribological Studies Using Nanoparticle Manipulation: Principles and Application to Structural Lubricity. *Friction* **2014**, *2*, 114–139. [CrossRef]
18. Zheng, Q.; Liu, Z. Experimental Advances in Superlubricity. *Friction* **2014**, *2*, 182–192. [CrossRef]
19. Baykara, M.Z.; Vazirisereshk, M.R.; Martini, A. Emerging Superlubricity: A Review of the State of the Art and Perspectives on Future Research. *Appl. Phys. Rev.* **2018**, *5*, 041102. [CrossRef]
20. Berman, D.; Erdemir, A.; Sumant, A.V. Approaches for Achieving Superlubricity in Two-Dimensional Materials. *ACS Nano* **2018**, *12*, 2122–2137. [CrossRef]
21. Zhang, X.; Ren, T.; Li, Z. Recent Advances of Two-Dimensional Lubricating Materials: From Tunable Tribological Properties to Applications. *J. Mater. Chem. A* **2023**, *11*, 9239–9269. [CrossRef]
22. Wang, J.; Ma, M.; Tosatti, E. Kinetic Friction of Structurally Superlubric 2D Material Interfaces. *J. Mech. Phys. Solids* **2023**, *180*, 105396. [CrossRef]
23. Wang, R.; Zhang, F.; Yang, K.; Xiong, Y.; Tang, J.; Chen, H.; Duan, M.; Li, Z.; Zhang, H.; Xiong, B. Review of Two-Dimensional Nanomaterials in Tribology: Recent Developments, Challenges and Prospects. *Adv. Colloid Interface Sci.* **2023**, *321*, 103004. [CrossRef] [PubMed]
24. Zhang, D.; Li, Z.; Klausen, L.H.; Li, Q.; Dong, M. Friction Behaviors of Two-Dimensional Materials at the Nanoscale. *Mater. Today Phys.* **2022**, *27*, 100771. [CrossRef]
25. Hod, O.; Meyer, E.; Zheng, Q.; Urbakh, M. Structural Superlubricity and Ultralow Friction across the Length Scales. *Nature* **2018**, *563*, 485–492. [CrossRef] [PubMed]
26. Yuan, J.; Yang, R.; Zhang, G. Structural Superlubricity in 2D van Der Waals Heterojunctions. *Nanotechnology* **2022**, *33*, 102002. [CrossRef] [PubMed]
27. Huang, K.; Qin, H.; Zhang, S.; Li, Q.; Ouyang, W.; Liu, Y. The Origin of Moiré-Level Stick-Slip Behavior on Graphene/*h*-BN Heterostructures. *Adv. Funct. Mater.* **2022**, *32*, 2204209. [CrossRef]
28. Mate, C.M.; McClelland, G.M.; Erlandsson, R.; Chiang, S. Atomic-Scale Friction of a Tungsten Tip on a Graphite Surface. *Phys. Rev. Lett.* **1987**, *59*, 1942–1945. [CrossRef] [PubMed]
29. Belim, S.V.; Tikhomirov, I.V.; Bychkov, I.V. Simulation of Epitaxial Film–Substrate Interaction Potential. *Coatings* **2022**, *12*, 853. [CrossRef]
30. Hirano, M.; Shinjo, K. Superlubricity and Frictional Anisotropy. *Wear* **1993**, *168*, 121–125. [CrossRef]
31. Claerbout, V.E.P.; Polcar, T.; Nicolini, P. Superlubricity Achieved for Commensurate Sliding: MoS_2 Frictional Anisotropy in Silico. *Comput. Mater. Sci.* **2019**, *163*, 17–23. [CrossRef]
32. Levita, G.; Cavaleiro, A.; Molinari, E.; Polcar, T.; Righi, M.C. Sliding Properties of MoS_2 Layers: Load and Interlayer Orientation Effects. *J. Phys. Chem. C* **2014**, *118*, 13809–13816. [CrossRef]
33. Dienwiebel, M.; Verhoeven, G.S.; Pradeep, N.; Frenken, J.W.M.; Heimberg, J.A.; Zandbergen, H.W. Superlubricity of Graphite. *Phys. Rev. Lett.* **2004**, *92*, 126101. [CrossRef]
34. Song, Y.; Qu, C.; Ma, M.; Zheng, Q. Structural Superlubricity Based on Crystalline Materials. *Small* **2020**, *16*, 1903018. [CrossRef] [PubMed]

35. Liu, Z.; Yang, J.; Grey, F.; Liu, J.Z.; Liu, Y.; Wang, Y.; Yang, Y.; Cheng, Y.; Zheng, Q. Observation of Microscale Superlubricity in Graphite. *Phys. Rev. Lett.* **2012**, *108*, 205503. [CrossRef]
36. Konrad, J.; Gnecco, E.; Dietzel, D.; Schirmeisen, A. Anisotropy of Nanoscale Friction: Influence of Lattice Structure, Temperature, and Wear. *Phys. Rev. B* **2023**, *107*, 195438. [CrossRef]
37. Wang, D.; Chen, G.; Li, C.; Cheng, M.; Yang, W.; Wu, S.; Xie, G.; Zhang, J.; Zhao, J.; Lu, X.; et al. Thermally Induced Graphene Rotation on Hexagonal Boron Nitride. *Phys. Rev. Lett.* **2016**, *116*, 126101. [CrossRef]
38. Filippov, A.E.; Dienwiebel, M.; Frenken, J.W.M.; Klafter, J.; Urbakh, M. Torque and Twist against Superlubricity. *Phys. Rev. Lett.* **2008**, *100*, 046102. [CrossRef]
39. Song, Y.; Mandelli, D.; Hod, O.; Urbakh, M.; Ma, M.; Zheng, Q. Robust Microscale Superlubricity in Graphite/Hexagonal Boron Nitride Layered Heterojunctions. *Nat. Mater.* **2018**, *17*, 894–899. [CrossRef]
40. Kabengele, T.; Johnson, E.R. Theoretical Modeling of Structural Superlubricity in Rotated Bilayer Graphene, Hexagonal Boron Nitride, Molybdenum Disulfide, and Blue Phosphorene. *Nanoscale* **2021**, *13*, 14399–14407. [CrossRef]
41. Ru, G.; Qi, W.; Wei, Y.; Tang, K.; Xue, T. Superlubricity in Bilayer Isomeric Tellurene and Graphene/Tellurene van Der Waals Heterostructures. *Tribol. Int.* **2021**, *159*, 106974. [CrossRef]
42. Liu, L.; Zhou, M.; Jin, L.; Li, L.; Mo, Y.; Su, G.; Li, X.; Zhu, H.; Tian, Y. Recent Advances in Friction and Lubrication of Graphene and Other 2D Materials: Mechanisms and Applications. *Friction* **2019**, *7*, 199–216. [CrossRef]
43. Ruan, X.; Shi, J.; Wang, X.; Wang, W.Y.; Fan, X.; Zhou, F. Robust Superlubricity and Moiré Lattice's Size Dependence on Friction between Graphdiyne Layers. *ACS Appl. Mater. Interfaces* **2021**, *13*, 40901–40908. [CrossRef] [PubMed]
44. Bao, H.; Miao, Y.; Li, Y.; Bai, H.; Ma, F. Unveiling the Moiré Pattern Evolution and Superlubricity in Twisted Bilayer 2D Phosphorene at Atomistic Scale. *Appl. Surf. Sci.* **2022**, *606*, 154796. [CrossRef]
45. Ouyang, J.-H.; Li, Y.-F.; Zhang, Y.-Z.; Wang, Y.-M.; Wang, Y.-J. High-Temperature Solid Lubricants and Self-Lubricating Composites: A Critical Review. *Lubricants* **2022**, *10*, 177. [CrossRef]
46. Chen, X.; Li, J. Superlubricity of Carbon Nanostructures. *Carbon* **2020**, *158*, 1–23. [CrossRef]
47. Qu, C.; Shi, S.; Ma, M.; Zheng, Q. Rotational Instability in Superlubric Joints. *Phys. Rev. Lett.* **2019**, *122*, 246101. [CrossRef] [PubMed]
48. Oyarzún-Aravena, A.M.; Gottschalk-Ojeda, C.; Moya-Barría, I.; Vallejos-Burgos, F. Edge Type Effect in the Gasification Mechanism of Graphene Clusters with H_2O and/or CO_2: Armchair vs. Zigzag. *Carbon* **2022**, *193*, 412–427. [CrossRef]
49. Qu, C.; Wang, K.; Wang, J.; Gongyang, Y.; Carpick, R.W.; Urbakh, M.; Zheng, Q. Origin of Friction in Superlubric Graphite Contacts. *Phys. Rev. Lett.* **2020**, *125*, 126102. [CrossRef]
50. Yan, W.; Bhuiyan, F.H.; Tang, C.; Wei, L.; Jiang, Y.; Jang, S.; Liu, Y.; Wu, J.; Wang, W.; Wang, Y.; et al. Understanding and Preventing Lubrication Failure at the Carbon Atomic Steps. *Small* **2023**, *19*, 2301515. [CrossRef]
51. Gong, P.; Li, J.; Wang, J.; Wu, W.; Li, C.; Wang, D.; Shi, J.; Liu, J.; Zhou, F.; Liu, W. Controlled Growing of Graphdiyne Film for Friction Reduction and Antiwear. *ACS Nano* **2023**, *17*, 8252–8261. [CrossRef] [PubMed]
52. Li, G.; Li, Y.; Liu, H.; Guo, Y.; Li, Y.; Zhu, D. Architecture of Graphdiyne Nanoscale Films. *Chem. Commun.* **2010**, *46*, 3256. [CrossRef] [PubMed]
53. Zhu, Z.; Cai, X.; Yi, S.; Chen, J.; Dai, Y.; Niu, C.; Guo, Z.; Xie, M.; Liu, F.; Cho, J.-H.; et al. Multivalency-Driven Formation of Te-Based Monolayer Materials: A Combined First-Principles and Experimental Study. *Phys. Rev. Lett.* **2017**, *119*, 106101. [CrossRef] [PubMed]
54. Özoğul, A.; İpek, S.; Durgun, E.; Baykara, M.Z. Structural Superlubricity of Platinum on Graphite under Ambient Conditions: The Effects of Chemistry and Geometry. *Appl. Phys. Lett.* **2017**, *111*, 211602. [CrossRef]
55. Dietzel, D.; Feldmann, M.; Schwarz, U.D.; Fuchs, H.; Schirmeisen, A. Scaling Laws of Structural Lubricity. *Phys. Rev. Lett.* **2013**, *111*, 235502. [CrossRef] [PubMed]
56. Cihan, E.; İpek, S.; Durgun, E.; Baykara, M.Z. Structural Lubricity under Ambient Conditions. *Nat. Commun.* **2016**, *7*, 12055. [CrossRef] [PubMed]
57. Kaul, A.B. Two-Dimensional Layered Materials: Structure, Properties, and Prospects for Device Applications. *J. Mater. Res.* **2014**, *29*, 348–361. [CrossRef]
58. Li, H.; Wang, J.; Gao, S.; Chen, Q.; Peng, L.; Liu, K.; Wei, X. Superlubricity between MoS_2 Monolayers. *Adv. Mater.* **2017**, *29*, 1701474. [CrossRef] [PubMed]
59. Li, H.; Ju, S.; Ji, L.; Liu, X.; Zhou, H.; Chen, J.; Zhao, X. Superlubricity of Molybdenum Disulfide Film. *Surf. Sci. Technol.* **2023**, *1*, 27. [CrossRef]
60. Martin, J.M.; Pascal, H.; Donnet, C.; Le Mogne, T.; Loubet, J.L.; Epicier, T. Superlubricity of MoS_2: Crystal Orientation Mechanisms. *Surf. Coat. Technol.* **1994**, *68–69*, 427–432. [CrossRef]
61. Martin, J.M.; Donnet, C.; Le Mogne, T.; Epicier, T. Superlubricity of Molybdenum Disulphide. *Phys. Rev. B* **1993**, *48*, 10583–10586. [CrossRef] [PubMed]
62. Dietzel, D.; Brndiar, J.; Štich, I.; Schirmeisen, A. Limitations of Structural Superlubricity: Chemical Bonds versus Contact Size. *ACS Nano* **2017**, *11*, 7642–7647. [CrossRef] [PubMed]
63. Li, M.; Shi, J.; Liu, L.; Yu, P.; Xi, N.; Wang, Y. Experimental Study and Modeling of Atomic-Scale Friction in Zigzag and Armchair Lattice Orientations of MoS_2. *Sci. Technol. Adv. Mater.* **2016**, *17*, 189–199. [CrossRef] [PubMed]

64. Wu, S.; Meng, Z.; Tao, X.; Wang, Z. Superlubricity of Molybdenum Disulfide Subjected to Large Compressive Strains. *Friction* **2022**, *10*, 209–216. [CrossRef]
65. Büch, H.; Rossi, A.; Forti, S.; Convertino, D.; Tozzini, V.; Coletti, C. Superlubricity of Epitaxial Monolayer WS_2 on Graphene. *Nano Res.* **2018**, *11*, 5946–5956. [CrossRef]
66. Li, P.; Yi Wang, W.; Zou, C.; Gao, X.; Wang, J.; Fan, X.; Song, H.; Li, J. Lattice Distortion Optimized Hybridization and Superlubricity of MoS_2/$MoSe_2$ Heterointerfaces via Moiré Patterns. *Appl. Surf. Sci.* **2023**, *613*, 155760. [CrossRef]
67. Roy, S.; Zhang, X.; Puthirath, A.B.; Meiyazhagan, A.; Bhattacharyya, S.; Rahman, M.M.; Babu, G.; Susarla, S.; Saju, S.K.; Tran, M.K.; et al. Structure, Properties and Applications of Two-Dimensional Hexagonal Boron Nitride. *Adv. Mater.* **2021**, *33*, 2101589. [CrossRef]
68. Leven, I.; Krepel, D.; Shemesh, O.; Hod, O. Robust Superlubricity in Graphene/h -BN Heterojunctions. *J. Phys. Chem. Lett.* **2013**, *4*, 115–120. [CrossRef]
69. Liao, M.; Silva, A.; Du, L.; Nicolini, P.; Claerbout, V.E.P.; Kramer, D.; Yang, R.; Shi, D.; Polcar, T.; Zhang, G. Twisting Dynamics of Large Lattice-Mismatch van Der Waals Heterostructures. *ACS Appl. Mater. Interfaces* **2023**, *15*, 19616–19623. [CrossRef]
70. Wang, K.; Qu, C.; Wang, J.; Quan, B.; Zheng, Q. Characterization of a Microscale Superlubric Graphite Interface. *Phys. Rev. Lett.* **2020**, *125*, 026101. [CrossRef]
71. Koren, E.; Duerig, U. Moiré Scaling of the Sliding Force in Twisted Bilayer Graphene. *Phys. Rev. B* **2016**, *94*, 045401. [CrossRef]
72. Minkin, A.S.; Lebedeva, I.V.; Popov, A.M.; Knizhnik, A.A. Atomic-Scale Defects Restricting Structural Superlubricity: Ab Initio Study Study on the Example of the Twisted Graphene Bilayer. *Phys. Rev. B* **2021**, *104*, 075444. [CrossRef]
73. Liu, J.; Yang, X.; Fang, H.; Yan, W.; Ouyang, W.; Liu, Z. In Situ Twistronics: A New Platform Based on Superlubricity. *Adv. Mater.* **2023**, 2305072. [CrossRef] [PubMed]
74. Deng, H.; Ma, M.; Song, Y.; He, Q.; Zheng, Q. Structural Superlubricity in Graphite Flakes Assembled under Ambient Conditions. *Nanoscale* **2018**, *10*, 14314–14320. [CrossRef] [PubMed]
75. Huang, X.; Li, T.; Wang, J.; Xia, K.; Tan, Z.; Peng, D.; Xiang, X.; Liu, B.; Ma, M.; Zheng, Q. Robust Microscale Structural Superlubricity between Graphite and Nanostructured Surface. *Nat. Commun.* **2023**, *14*, 2931. [CrossRef] [PubMed]
76. Peng, D.; Wang, J.; Jiang, H.; Zhao, S.; Wu, Z.; Tian, K.; Ma, M.; Zheng, Q. 100 Km Wear-Free Sliding Achieved by Microscale Superlubric Graphite/DLC Heterojunctions under Ambient Conditions. *Natl. Sci. Rev.* **2022**, *9*, nwab109. [CrossRef] [PubMed]
77. Li, Q.; Dong, Y.; Perez, D.; Martini, A.; Carpick, R.W. Speed Dependence of Atomic Stick-Slip Friction in Optimally Matched Experiments and Molecular Dynamics Simulations. *Phys. Rev. Lett.* **2011**, *106*, 126101. [CrossRef] [PubMed]
78. Braun, O.M. Bridging the Gap Between the Atomic-Scale and Macroscopic Modeling of Friction. *Tribol. Lett.* **2010**, *39*, 283–293. [CrossRef]
79. Brenner, D.W.; Shenderova, O.A.; Harrison, J.A.; Stuart, S.J.; Ni, B.; Sinnott, S.B. A Second-Generation Reactive Empirical Bond Order (REBO) Potential Energy Expression for Hydrocarbons. *J. Phys. Condens. Matter* **2002**, *14*, 783–802. [CrossRef]
80. Yan, S.; He, L. Adhesive Force between a Spherical Rigid Particle and an Incompressible Elastic Substrate. *Mech. Mater.* **2012**, *49*, 66–71. [CrossRef]
81. Feng, S.; Xu, Z. Robustness of Structural Superlubricity beyond Rigid Models. *Friction* **2022**, *10*, 1382–1392. [CrossRef]
82. Kolmogorov, A.N.; Crespi, V.H. Registry-Dependent Interlayer Potential for Graphitic Systems. *Phys. Rev. B* **2005**, *71*, 235415. [CrossRef]
83. Daw, M.S.; Baskes, M.I. Embedded-Atom Method: Derivation and Application to Impurities, Surfaces, and Other Defects in Metals. *Phys. Rev. B* **1984**, *29*, 6443–6453. [CrossRef]
84. Liao, M.; Nicolini, P.; Du, L.; Yuan, J.; Wang, S.; Yu, H.; Tang, J.; Cheng, P.; Watanabe, K.; Taniguchi, T.; et al. UItra-Low Friction and Edge-Pinning Effect in Large-Lattice-Mismatch van Der Waals Heterostructures. *Nat. Mater.* **2022**, *21*, 47–53. [CrossRef]
85. Jiang, J.-W.; Park, H.S. A Gaussian Treatment for the Friction Issue of Lennard-Jones Potential in Layered Materials: Application to Friction between Graphene, MoS_2, and Black Phosphorus. *J. Appl. Phys.* **2015**, *117*, 124304. [CrossRef]
86. Wang, S.; Zhao, L.; Liu, Y. Large-Scale Simulation of Graphene and Structural Superlubricity with Improved Smoothed Molecular Dynamics Method. *Comput. Methods Appl. Mech. Eng.* **2022**, *392*, 114644. [CrossRef]
87. Gao, E.; Wu, B.; Wang, Y.; Jia, X.; Ouyang, W.; Liu, Z. Computational Prediction of Superlubric Layered Heterojunctions. *ACS Appl. Mater. Interfaces* **2021**, *13*, 33600–33608. [CrossRef]
88. Losi, G.; Restuccia, P.; Righi, M.C. Superlubricity in Phosphorene Identified by Means of Ab Initio Calculations. *2D Mater.* **2020**, *7*, 025033. [CrossRef]
89. Cheng, Z.; Feng, H.; Sun, J.; Lu, Z.; He, Q.-C. Strain-Driven Superlubricity of Graphene/Graphene in Commensurate Contact. *Adv. Mater. Interfaces* **2023**, *10*, 2202062. [CrossRef]
90. Liu, S.-W.; Wang, H.-P.; Xu, Q.; Ma, T.-B.; Yu, G.; Zhang, C.; Geng, D.; Yu, Z.; Zhang, S.; Wang, W.; et al. Robust Microscale Superlubricity under High Contact Pressure Enabled by Graphene-Coated Microsphere. *Nat. Commun.* **2017**, *8*, 14029. [CrossRef]
91. Li, J.; Li, J.; Luo, J. Superlubricity of Graphite Sliding against Graphene Nanoflake under Ultrahigh Contact Pressure. *Adv. Sci.* **2018**, *5*, 1800810. [CrossRef]
92. Li, J.; Li, J.; Chen, X.; Liu, Y.; Luo, J. Microscale Superlubricity at Multiple Gold–Graphite Heterointerfaces under Ambient Conditions. *Carbon* **2020**, *161*, 827–833. [CrossRef]
93. Yan, W.; Ouyang, W.; Liu, Z. Origin of Frictional Scaling Law in Circular Twist Layered Interfaces: Simulations and Theory. *J. Mech. Phys. Solids* **2023**, *170*, 105114. [CrossRef]

94. de Wijn, A.S. (In)Commensurability, Scaling, and Multiplicity of Friction in Nanocrystals and Application to Gold Nanocrystals on Graphite. *Phys. Rev. B* **2012**, *86*, 085429. [CrossRef]
95. Wang, J.; Cao, W.; Song, Y.; Qu, C.; Zheng, Q.; Ma, M. Generalized Scaling Law of Structural Superlubricity. *Nano Lett.* **2019**, *19*, 7735–7741. [CrossRef] [PubMed]
96. Bai, H.; Bao, H.; Li, Y.; Xu, H.; Li, S.; Ma, F. Moiré Pattern Based Universal Rules Governing Interfacial Superlubricity: A Case of Graphene. *Carbon* **2022**, *191*, 28–35. [CrossRef]
97. Lee, C.; Li, Q.; Kalb, W.; Liu, X.-Z.; Berger, H.; Carpick, R.W.; Hone, J. Frictional Characteristics of Atomically Thin Sheets. *Science* **2010**, *328*, 76–80. [CrossRef]
98. Chen, Y.; Guan, Z.; Liu, J.; Yang, W.; Wang, H. Anomalous Layer-Dependent Lubrication on Graphene-Covered Substrate: Competition between Adhesion and Plasticity. *Appl. Surf. Sci.* **2022**, *598*, 153762. [CrossRef]
99. Morovati, V.; Xue, Z.; Liechti, K.M.; Huang, R. Interlayer Coupling and Strain Localization in Small-Twist-Angle Graphene Flakes. *Extreme Mech. Lett.* **2022**, *55*, 101829. [CrossRef]
100. Bai, H.; Bao, H.; Li, Y.; Xu, H.; Li, S.; Ma, F. One-Dimensional Strain Solitons Manipulated Superlubricity on Graphene Interface. *J. Phys. Chem. Lett.* **2022**, *13*, 7261–7268. [CrossRef]
101. Sharp, T.A.; Pastewka, L.; Robbins, M.O. Elasticity Limits Structural Superlubricity in Large Contacts. *Phys. Rev. B* **2016**, *93*, 121402. [CrossRef]
102. Rejhon, M.; Lavini, F.; Khosravi, A.; Shestopalov, M.; Kunc, J.; Tosatti, E.; Riedo, E. Relation between Interfacial Shear and Friction Force in 2D Materials. *Nat. Nanotechnol.* **2022**, *17*, 1280–1287. [CrossRef] [PubMed]
103. Monti, J.M.; Robbins, M.O. Sliding Friction of Amorphous Asperities on Crystalline Substrates: Scaling with Contact Radius and Substrate Thickness. *ACS Nano* **2020**, *14*, 16997–17003. [CrossRef] [PubMed]
104. Gao, Y.; Kim, S.; Zhou, S.; Chiu, H.-C.; Nélias, D.; Berger, C.; de Heer, W.; Polloni, L.; Sordan, R.; Bongiorno, A.; et al. Elastic Coupling between Layers in Two-Dimensional Materials. *Nat. Mater.* **2015**, *14*, 714–720. [CrossRef]
105. Yankowitz, M. Unravelling the Magic of Twisted Trilayer Graphene. *Nat. Mater.* **2023**, *22*, 286–287. [CrossRef] [PubMed]
106. Yan, W.; Shui, L.; Ouyang, W.; Liu, Z. Thermodynamic Model of Twisted Bilayer Graphene: Entropy Matters. *J. Mech. Phys. Solids* **2022**, *167*, 104972. [CrossRef]
107. Liu, Z.; Vilhena, J.G.; Hinaut, A.; Scherb, S.; Luo, F.; Zhang, J.; Glatzel, T.; Gnecco, E.; Meyer, E. Moiré-Tile Manipulation-Induced Friction Switch of Graphene on a Platinum Surface. *Nano Lett.* **2023**, *23*, 4693–4697. [CrossRef]
108. Bai, H.; Zou, G.; Bao, H.; Li, S.; Ma, F.; Gao, H. Deformation Coupled Moiré Mapping of Superlubricity in Graphene. *ACS Nano* **2023**, *17*, 12594–12602. [CrossRef]
109. Song, Y.; Hinaut, A.; Scherb, S.; Pellmont, Y.; Pawlak, R.; Huang, S.; Liu, Z.; Glatzel, T.; Meyer, E. Observation of Robust Superlubricity of MoS_2 on Au (111) in Ultrahigh Vacuum. *Appl. Surf. Sci.* **2022**, *601*, 154230. [CrossRef]
110. Liu, Y.; Ren, J.; Kong, D.; Shan, G.; Dou, K. Edge-Pinning Effect of Graphene Nanoflakes Sliding atop Graphene. *Mater. Today Phys.* **2023**, *38*, 101266. [CrossRef]
111. Sun, S.; Ru, G.; Qi, W.; Liu, W. Molecular Dynamics Study of the Robust Superlubricity in Penta-Graphene van Der Waals Layered Structures. *Tribol. Int.* **2023**, *177*, 107988. [CrossRef]
112. Kim, J.S.; Warner, J.H.; Robertson, A.W.; Kirkland, A.I. Formation of Klein Edge Doublets from Graphene Monolayers. *ACS Nano* **2015**, *9*, 8916–8922. [CrossRef] [PubMed]
113. Chen, Z.; Kim, S.H. Measuring Nanoscale Friction at Graphene Step Edges. *Friction* **2020**, *8*, 802–811. [CrossRef]
114. Levita, G.; Restuccia, P.; Righi, M. Graphene and MoS_2 Interacting with Water: A Comparison by Ab Initio Calculations. *Carbon* **2016**, *107*, 878–884. [CrossRef]
115. Dong, C.; Jiang, D.; Fu, Y.; Wang, D.; Wang, Q.; Weng, L.; Hu, M.; Gao, X.; Sun, J. Macro-Superlubricity in Sputtered MoS_2-Based Films by Decreasing Edge Pinning Effect. *Friction* **2024**, *12*, 52–63. [CrossRef]
116. Song, Y.; Gao, X.; Hinaut, A.; Scherb, S.; Huang, S.; Hod, O.; Urbakh, M.; Meyer, E. Velocity Dependence of Moiré Friction. *Nano Lett.* **2022**, *22*, 9529–9536. [CrossRef]
117. Sun, J.; Zhang, Y.; Lu, Z.; Li, Q.; Xue, Q.; Du, S.; Pu, J.; Wang, L. Superlubricity Enabled by Pressure-Induced Friction Collapse. *J. Phys. Chem. Lett.* **2018**, *9*, 2554–2559. [CrossRef] [PubMed]
118. He, Y.; She, D.; Liu, Z.; Wang, X.; Zhong, L.; Wang, C.; Wang, G.; Mao, S.X. Atomistic Observation on Diffusion-Mediated Friction between Single-Asperity Contacts. *Nat. Mater.* **2022**, *21*, 173–180. [CrossRef]
119. Wang, K. Structural Superlubricity with a Contaminant-Rich Interface. *J. Mech. Phys. Solids* **2022**, *169*, 105063. [CrossRef]
120. Zhang, Z.; Du, Y.; Huang, S.; Meng, F.; Chen, L.; Xie, W.; Chang, K.; Zhang, C.; Lu, Y.; Lin, C.; et al. Macroscale Superlubricity Enabled by Graphene-Coated Surfaces. *Adv. Sci.* **2020**, *7*, 1903239. [CrossRef]
121. Li, P.; Ju, P.; Ji, L.; Li, H.; Liu, X.; Chen, L.; Zhou, H.; Chen, J. Toward Robust Macroscale Superlubricity on Engineering Steel Substrate. *Adv. Mater.* **2020**, *32*, 2002039. [CrossRef] [PubMed]
122. Androulidakis, C.; Koukaras, E.N.; Paterakis, G.; Trakakis, G.; Galiotis, C. Tunable Macroscale Structural Superlubricity in Two-Layer Graphene via Strain Engineering. *Nat. Commun.* **2020**, *11*, 1595. [CrossRef] [PubMed]
123. Wang, K.; Ouyang, W.; Cao, W.; Ma, M.; Zheng, Q. Robust Superlubricity by Strain Engineering. *Nanoscale* **2019**, *11*, 2186–2193. [CrossRef] [PubMed]
124. Li, R.; Sun, C.; Yang, X.; Wang, Y.; Gao, K.; Zhang, J.; Li, J. Toward High Load-Bearing, Ambient Robust and Macroscale Structural Superlubricity through Contact Stress Dispersion. *Chem. Eng. J.* **2022**, *431*, 133548. [CrossRef]

125. Yang, X.; Li, R.; Wang, Y.; Zhang, J. Tunable, Wide-Temperature, and Macroscale Superlubricity Enabled by Nanoscale Van Der Waals Heterojunction-to-Homojunction Transformation. *Adv. Mater.* **2023**, *35*, 2303580. [CrossRef] [PubMed]
126. Ge, X.; Chai, Z.; Shi, Q.; Liu, Y.; Wang, W. Graphene Superlubricity: A Review. *Friction* **2023**, *11*, 1953–1973. [CrossRef]
127. Yuan, W.; Yao, Y.; Keer, L.; Jiao, Y.; Yu, J.; Li, Q.; Feng, X.-Q. 3D-Printed Biomimetic Surface Structures with Abnormal Friction Properties. Extreme Mech. *Lett.* **2019**, *26*, 46–52.
128. Zhao, Y.; Mei, H.; Chang, P.; Chen, C.; Cheng, L.; Dassios, K.G. Infinite Approaching Superlubricity by Three-Dimensional Printed Structures. *ACS Nano* **2021**, *15*, 240–257. [CrossRef] [PubMed]
129. Zhao, Y.; Mei, H.; Chang, P.; Yang, Y.; Huang, W.; Liu, Y.; Cheng, L.; Zhang, L. 3D-Printed Topological $MoS_2/MoSe_2$ Heterostructures for Macroscale Superlubricity. ACS Appl. *Mater. Interfaces* **2021**, *13*, 34984–34995. [CrossRef]
130. Zhai, W.; Zhou, K. Nanomaterials in Superlubricity. *Adv. Funct. Mater.* **2019**, *29*, 1806395. [CrossRef]
131. Yuan, S.; Chen, X.; Zhang, C. Reducing Friction by Control of Isoelectric Point: A Potential Method to Design Artificial Cartilage. *Adv. Mater. Interfaces* **2020**, *7*, 2000485. [CrossRef]